POLYTECHNIC UNIVERSITY OF TURIN

Master degree course in Physics of Complex Systems

Master Degree Thesis

Field enhancement in metal nanoparticles for hot electrons generation rate

from single particle's shape to disordered 2d arrays

POLITECNICO
DI TORINO

Supervisors:
Professor Arianna Montorsi,
Polytechnic University of Turin
Professor Andrea Fratalocchi,
King Abdullah University of Science and Technology

Candidate:
Alessandro Mirigaldi,
239773

ACADEMIC YEAR: 2017/2018

a mia madre, che non mi ha mai trattenuto e sempre spinto a partire
a mio padre, che mi ha sempre sostenuto come una roccia sostiene il viaggiatore
a Valerio e Marcella, che mi hanno fatto sentire a casa
nonostante sia stato piú che mai lontano da casa
a Daniele, che mi ha ricordato che casa é sempre li ad accogliermi

Contents

Chapter 1

Abstract

In recent years, the prediction about the shortage of fossil oil, the increase of its extraction price and the environmental damage caused by its based product has been the reason of a novel wave of research in the renewable energy-s field. Among the many renewable sources hydrogen has became quite popular. Indeed, hydrogen combustion give as results heat and water, that can be again dissociated into oxygen and hydrogen.

$$2H_2 + O_2 \Longleftrightarrow 2H_2O + \quad energy$$

Hydrogen can become an efficient fuel in everyday future life but there are some issues related to this particular use. It should be accumulated in his liquid form which is extremely flammable and the currently used hydrogen production methods, namely the dissociation of a water molecule into hydrogen and oxygen, are energetically expensive. The most common hydrogen production method is steam reforming from hydrocarbons. This method releases CO_2 during the process and does not self-sustain itself so an external power supply is needed. Generally this power supply is obtained by combustion of other fuels[4]. An alternative method to produce hydrogen is the photon-induced hydrolysis, that is an hydrolysis process induced by solar energy.
Hydrolysis has gained a lot of attention in recent years because it would allow to directly convert solar energy, which is an almost infinite source of energy, into the chemical energy needed to break down water molecules[8]. The basic idea is to use the photogenerated hot electrons inside metal nanostructures to drive the hydrolysis in surface molecules on top of the nanostructure itself. When an electromagnetic wave impinges a metallic surface the electrons inside the metal jump to excited states creating surface plasmons, which are collective oscillations of the electron cloud. Due to the crystal momentum conservation, these electrons don't have enough energy to drive an hydrolysis reaction. However, if metallic nanocrystals are used then hot carriers make their appearance. In this case the crystal momentum is no longer conserved and the electrons can assume energy in the range $E_F < \epsilon < E_F + \hbar\omega$ where E_F is the Fermi level of the considered metal and ω is the pulsation of the incident light. In the same way energetic holes in the range $E_F - \hbar\omega < \epsilon\ E_F$ are created. These are the so called hot carriers which can drive the hydrolysis of water surface molecules[14] .
It is known that the density of photogenerated hot carriers is strongly dependent on material and shape of the nanostructure. The aim of this work is to further investigate the shape dependence of the photolysis and understand how this process can be optimized by mean of numerical simulations. It has been shown experimentally that the presence of the so called hot spots further enhances the

hot electron generation rates [12]. Therefore, firstly the properties of the elementary geometries, in term of broadness of the photonic surface density of states as well as hot electron generation rate, both as function of the wavelength of the impinging wave, are examined by mean of a first set of finite difference time domain simulations. The next natural step is the study of 2d arrays of nanoparticles, which are of practical interest when it comes to hydrogen generation. It is indeed well known that the introduction of disorder in optical media gives rise to a strong localization of light [7] just like the disorder in solid's lattice potentials gives rise to the so called Anderson localization. Inspired by that, among all possible kind of 2d array, 2D disordered arrays, in which either the size of the nanoparticles or their position is chosen according to some probability distribution, have been studied. To further understand the role of disorder in the enhancement of the electromagnetic field needed for hydrogen generation, the localization length, which gives a measure of how the intensity of the electric field due to the introduction of randomness is localized at the nanoscale, has been computed in several 2d arrays. The analysis of this quantity indeed leads to find the parameters that better enhances the electromagnetic field. Finally, the hot electron generation rate has been computed for the array's geometry characterized by the found parameters, showing how the disorder plays a determinant role increasing the broadness of the hot electron generation rate of the whole system.
This thesis is organized as follows. Firstly, the theoretical framework of the hot electron generation rate is briefly recalled as well as the finite difference time domain method, which allows to numerically solve the Maxwell equations. Then, the results are presented. Firstly, the enhancement driven by single particles shapes is shown and various geometries compared. Then the effect of disorder on the surface photonic DOS and hot electron generation rate on 2d array of nanoparticles is then studied. Finally the surface photonic DOS and the hot electron generation rate for four different system are compared.

Chapter 2

Quantum theory of photogeneration of hot electrons in metallic nanostructures

2.1 Density matrix equation of motion

The simplest theoretical framework to study the hot carriers generation in plasmonic nanostructures is based on two approximation: the use of a free electron model for nanostructure's conduction electrons as well as a perturbative solution of the density matrix equation of motion. A nanostructure, from now on NS, in contact with a semiconductor of surface molecules, is considered. This theory is based on the equation of motion of the density matrix of the whole system, that is a classical electromagnetic perturbative field, the NS and the surrounding environment whose density matrix elements are:

$$\rho_{nm}(t) = \langle \Psi(t) | a_n^\dagger a_m | \Psi(t) \rangle \tag{2.1.0.1}$$

with $a_n^\dagger$,a_n the raising and lowering field operator and $\Psi(t)$ the many-body time depended wavefunction of the whole system.The equation of motion of the system reads[14]:

$$\hbar \frac{\partial \hat{\rho}}{\partial t} = i[\hat{\rho}, \hat{H}_0 + \hat{w}_{tun} + \hat{V}_{opt}] - \hat{\Gamma}(\hat{\rho}) \tag{2.1.0.2}$$

This is simply the equation of motion of the density matrix operator in the Heisemberg picture with the additional term $\hat{\Gamma}(\hat{\rho})$ which ensures the relaxation of the system towards the equilibrium density matrix, whose diagonal elements are given by the Fermi-Dirac distribution for the n-th state. The relaxation operator form must be chosen carefully, not to make the equation impossible to solve. In this case, a proper form is[11]:

$$\langle m | \hat{\Gamma}(\hat{\rho}) | n \rangle = \Gamma_{mn}(\rho_{mn} - \rho^0_{mn}) \tag{2.1.0.3}$$

$$\rho^0_{mn} = f(\epsilon_n)\delta_{m,n} \tag{2.1.0.4}$$

where $f(\epsilon_n)\delta_{m,n}$ is the Fermi-Dirac distribution and $\delta_{n,m}$ is the Kroneker delta
The electrons will mainly feel the confining potential of the NS, so these electrons will be treated

as free electrons described by the Hamiltonian $\hat{H}_0$. $\hat{w}_{tun}$ describes the tunnelling of electrons from the NS to the semiconductor or to surface molecules. The external field is assumed to be a monochromatic perturbation whose Hamiltonian is[11]

$$\hat{V}_{opt} = -e\hat{\phi}e^{-i\omega t} - e\hat{\phi}^* e^{i\omega t} \tag{2.1.0.5}$$

In components,the equation of motion reads:

$$\hbar\frac{\partial\rho_{nm}}{\partial t} = i\langle n|[\hat{\rho}, \hat{H}_0 + \hat{w}_{tun} + \hat{V}_{opt}]|m\rangle - \Gamma_{mn}(\rho_{mn} - \rho^0_{mn}) \tag{2.1.0.6}$$

A perturbative approach is involved to solve the set of equation of motion. It's solution for the diagonal elements is[11]

$$(\hbar\omega - \epsilon_m + \epsilon_n + i\Gamma_{mn})\rho^a_{mn} + \sum_\alpha(\rho_{m\alpha}w_{\alpha n} - w_{n\alpha}\rho_{\alpha m}) = -e\phi^a_{nm}(f(\epsilon_m) - f(\epsilon_n)) \tag{2.1.0.7}$$

$$(\hbar\omega - \epsilon_m + \epsilon_n + i\Gamma_{mn})\rho^b_{mn} + \sum_\alpha(\rho_{m\alpha}w_{\alpha n} - w_{n\alpha}\rho_{\alpha m}) = -e\phi^b_{nm}(f(\epsilon_m) - f(\epsilon_n)) \tag{2.1.0.8}$$

with α a state of the semiconductor or surface molecule and

$$\phi^a_{nn'} = \langle n|\hat{\phi}|n'\rangle \qquad\qquad \phi^b_{nn'} = \langle n|\hat{\phi}^*|n'\rangle \tag{2.1.0.9}$$

For clarity's sake it is useful to neglect the tunnelling terms so that equations 2.1.0.7 and 2.1.0.8 give:

$$\begin{aligned}\rho^a_{nn'} &= e\phi_{nn'}\frac{f(\epsilon_{n'}) - f(\epsilon_n)}{\hbar\omega - \epsilon_n + \epsilon'_n + i\Gamma_{nn'}}\\ \rho^b_{nn'} &= e\phi^b_{nn'}\frac{f(\epsilon_{n'}) - f(\epsilon_n)}{-\hbar\omega - \epsilon_n + \epsilon'_n + i\Gamma_{nn'}}\end{aligned} \tag{2.1.0.10}$$

At the lowest order in the perturbation the diagonal elements are given by[11]

$$\delta\rho^0_{nn} = \rho_{nn} - f(\epsilon_n) = \frac{2e}{\Gamma_{nn}}Im(\sum_{n'}\rho^a_{nn'}\phi^b_{n'n} + \rho^b_{nn'}\phi^a_{n'n} + \sum_\alpha\rho_{n\alpha}w_{\alpha n}) \tag{2.1.0.11}$$

Using the expression for the non diagonal term of equation 2.1.0.10 equation 2.1.0.11 reads:

$$\begin{aligned}\delta\rho_{nn} &= \frac{2e^2}{\Gamma_{nn}}\sum_{n'}(f(\epsilon_{n'}) - f(\epsilon_n))K_{n,n'}\\ K_{n,n'} &= |\phi^a_{nn'}|^2\frac{\Gamma_{nn'}}{(\hbar\omega - \epsilon_n + \epsilon_{n'})^2 + \Gamma^2_{nn'}} + |\phi^b_{nn'}|^2\frac{\Gamma_{nn'}}{(\hbar\omega + \epsilon_n - \epsilon_{n'})^2 + \Gamma^2_{nn'}}\end{aligned} \tag{2.1.0.12}$$

It's worth to notice that in this perturbative approach the energy distribution of electrons is the equilibrium one, namely the Fermi distribution, plus a correction due to the perturbation. Being the system in a stationary state

$$\frac{i}{\hbar}\langle n|[\hat{\rho}, \hat{H}_0 + \hat{w}_{tun} + \hat{V}_{opt}]|m\rangle = \langle n|\hat{\Gamma}(\hat{\rho}|n\rangle$$

so one can define the n-th state generation rates G_n and its associated relaxation rate R_n as

$$\begin{aligned} \frac{dN_e}{dt} = G_n = \frac{i}{\hbar}\langle n|[\hat{\rho}, \hat{H}_0 + \hat{w}_{tun} + \hat{V}_{opt}]|m\rangle \\ R_n = \langle n|\hat{\Gamma}(\hat{\rho}|n\rangle \end{aligned} \tag{2.1.0.13}$$

Then, under the previous assumption, G_n and R_n can be rewritten as

$$G_n = \frac{2e^2}{\hbar}\sum_l (f(\epsilon_l) - f(\epsilon_n))K_{n,l}$$

$$R_n = \frac{\Gamma_{nn}}{\hbar}\delta\rho_{nn}$$

$$\delta\rho_{nn} = \frac{\hbar G_n}{\Gamma_{nn}}$$

Finally ,the generation rate's distribution per unit of energy can be computed as

$$\frac{d^2N}{dtd\epsilon} = \sum_n G_n\delta(\epsilon - \epsilon_n) \tag{2.1.0.14}$$

while the hot electrons distribution per unit of energy can be computed as

$$\begin{aligned} \delta\rho(\epsilon) = \frac{dN_e}{d\epsilon} = \sum_n \delta\rho_{nn}\delta(\epsilon - \epsilon_n) = \\ = \sum_n \frac{\hbar G_n}{\Gamma_{nn}}\delta(\epsilon - \epsilon_n) = \sum_n \frac{2e^2}{\Gamma_{nn}}\sum_l (f(\epsilon_l - f(\epsilon_n))K_{n,l} \end{aligned} \tag{2.1.0.15}$$

2.2 Hot electron distribution dependence on the nanostructure shape

In general, the result of equation 2.1.0.15 must be computed numerically for arbitrary nanostructures unless the geometry of the system is extremely simple as in case of a metal slab or a sphere. Already in case of a cubic geometry the hot electron distribution cannot be computed analytically. Generally it presents two main features: a symmetric peak around the Fermi energy and a symmetric couple of plateaux below and above the Fermi level[14]. The peaks corresponds to carriers not far from the Fermi energy while the plateaux corresponds to a constant hot carriers distribution. The hot carrier distribution in the plateaux region can be derived for an arbitrary shape and geometry directly from equation 2.1.0.15.
The hot carriers are mainly generated at the surface of the nanostructure, where the confining potential is predominant so the first thing to do is to computed the hot carrier distribution over a

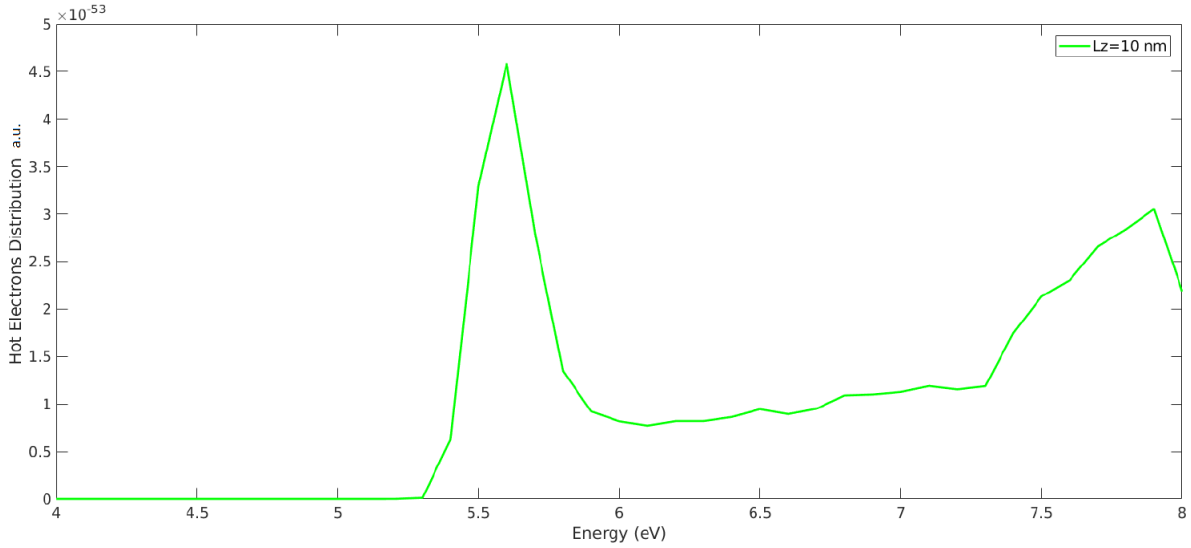

Figure 2.2.0.1: Hot electron generation rate computed for a gold nanoplatelet of width equal to 10 nm. If the holes were taken into account, the plot would be completely symmetric with respect to the Fermi energy. The main feature for the hot electron generation rate is the plateaux far from the Fermi energy, which is present only for metal nanocrystals, and the peak related to the less energetic electrons just around the Fermi energy.

surface ds. To do so, an extended metal slab is considered and its free electron are described by

$$\begin{aligned} \psi_{\mathbf{n}} &= (\frac{8}{L_x^2 L_z})^{1/2} sin(k_{n_x} x) sin(k_{n_y} y) sin(k_{n_z} z) \\ \mathbf{n} &= (n_x, n_y, n_z), \quad n_\alpha = 1, 2, 3... \\ k_{\mathbf{n}} &= (k_{n_x}, k_{n_y}, k_{n_z}) = (\frac{\pi n_x}{L_x}, \frac{\pi n_y}{L_x} \frac{\pi n_z}{L_z}) \\ \epsilon_n &= \frac{\hbar^2 \pi^2 (n_x^2 + n_y^2)}{2mL_x^2} + \frac{\hbar^2 \pi^2 n_z^2}{2mL_z^2} \end{aligned} \tag{2.2.0.1}$$

Still, the optical matrix element has to be computed. In this case L_z is assumed much smaller than L_x and L_y hence the interior field inside the platelet can be approximated by[11]

$$\mathbf{E}_\omega = \mathbf{E}_{inc} \gamma(\omega), \quad \gamma(\omega) = \frac{\epsilon_{ext}}{\epsilon_{met}(\omega)} \tag{2.2.0.2}$$

which is the field inside an infinite metal slab. For a metal slab in air, $\epsilon_{ext} = 1$. In the most simple case the incident radiation is a monochromatic wave so the optical matrix element reads:

$$\begin{aligned} \phi_{nm} &= \frac{\hbar^2}{2m(\epsilon_n - \epsilon_m)} \int \psi_{\mathbf{n}} (\mathbf{E}_\omega \cdot \nabla \psi_m) = \\ &= L_z E_{\omega,n} \frac{2}{\pi^2} (\frac{1}{(n_z - m_z)^2} - \frac{1}{(n_z + m_z)^2}) \delta_{n_z, m_x} \delta_{n_y m_y} \end{aligned} \tag{2.2.0.3}$$

where $E_{\omega,n}$ is the normal to the surface electric field modulus. Anyway, as we could notice, the in plane momentum is conserved and only the normal momentum undergoes a process of change. Equation 2.2.0.3 can be further simplified considering that only the electrons whose energy is around the Fermi energy could change their state. Hence, without losing generality, $n_z, m_z >> 1$ and

$$\begin{aligned} L_z E_{\omega,n} \frac{2}{\pi^2} \left(\frac{1}{(n_z - m_z)^2} - \frac{1}{(n_z + m_z)^2}\right) \delta_{n_z,m_x} \delta_{n_y m_y} \approx \\ \approx L_z E_{\omega,n} \frac{2}{\pi^2} \frac{1}{(n_z - m_z)^2} \delta_{n_x,m_x} \delta_{n_y,m_y} \end{aligned} \tag{2.2.0.4}$$

Considering that the hot carriers have an energy quite distant from the Fermi level, the factor $K_{n,l}$ can be further simplified:

$$\begin{aligned} K_{n,l} = |\phi^a_{nl}|^2 \frac{\Gamma}{(\hbar\omega - \epsilon_n + \epsilon_l)^2 + \Gamma^2} + |\phi^b_{nl}|^2 \frac{\Gamma}{(\hbar\omega - \epsilon_l + \epsilon_n)^2 + \Gamma^2} \simeq \\ \simeq |\phi^a_{nl}|^2 \pi\delta(\hbar\omega - \epsilon_n + \epsilon_l) + |\phi^b_{nl}|^2 \pi\delta(\hbar\omega - \epsilon_l + \epsilon_n) \end{aligned}$$

Under the previous assumption,

$$|\phi^a_{nl}|^2 = |\phi^b_{nl}|^2$$

As consequence, the double sum in equation 2.1.0.15 can be treated as an integral

$$\sum_{\mathbf{n},\mathbf{l}} = \sum_{n_{||},n_z,l_z} \simeq 2 \int_0^\infty dn_z \int_0^\infty dl_z \int_0^\infty d\mathbf{k}_{||} \frac{ds}{\pi^2}$$

$$\mathbf{k}_{||} = (k_{n_x}, k_{n_y})$$

where ds is the surface of the slab. The hot electron generation rate for the extended slab is then given by[11]:

$$\frac{dN_e}{dt d\epsilon} = \frac{4e^2 E_F^2}{\pi^2 \hbar} \frac{|E_{\omega,n}|^2}{(\hbar\omega)^4} ds \tag{2.2.0.5}$$

Actually, equation 2.2.0.5 takes into account both the normal surfaces. In order to get the hot electron rate it must be divided by a factor two to consider only one surface. Then one should integrate over the surface of the whole nanostructure. Hence, the hot electron distribution per unit of energy and time reads[12]:

$$\delta\rho(\epsilon) = \frac{2e^2 E_F^2}{\pi^2 \hbar} \int_{S_{NS}} \frac{|E_{\omega,n}|^2}{(\hbar\omega)^4} \qquad E_F + \delta E_b < \epsilon < E_F + \hbar\omega \tag{2.2.0.6}$$

while the hot holes distribution reads[12]

$$\delta\rho(\epsilon) = -\frac{2e^2 E_F^2}{\pi^2 \hbar} \int_{S_{NS}} \frac{|E_{\omega,n}|^2}{(\hbar\omega)^4} \qquad E_F - \hbar\omega < \epsilon < E_F - \delta E_b \tag{2.2.0.7}$$

This is not surprising since the excited carrier distribution must be a globally symmetric function. So, from equation 2.2.0.6 it is clear how the hot electrons distribution depends heavily on the particular choice of geometry, material and use of the device. Indeed, δE_b is related to the minimum energy an hot electron must have to overcome a barrier, just like in a Schottky barrier or to take

part to a chemical process with surface molecules, the material dependence is due the relaxation rate and Fermi energy and, eventually, the shape dependence comes from the surface integral of the electric field. The derivation of the hot carrier generation rate has been done, up to now, using the quasistatic approximation[5] within a perturbative approach which takes into account terms up to the first order expansion hence the electric field on the surface of the nanosphere would share the same frequency of the exciting field. As consequence a relevant quantity is the average value over an optical cycle of the hot carrier generation rate which could be obtained just by considering $< |E_{\omega,n}|^2 >$ instead of $|E_{\omega,n}|^2$ where

$$< A(t) >= \int_{optical\ cycle} dt A(t)$$

for any generic time dependent quantity.

Nanosphere

One of the few geometries analytically treatable is the spherical one. The internal electric field for

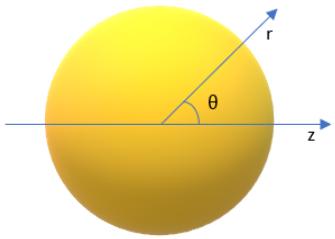

Figure 2.2.0.2: Nanosphere in the quasi static approximation. The azimuthal symmetry of the problem makes the potential, both internal and external, described only by θ and r

a nanosphere of radius a_0 in the quasi static approximation, taking $\hat{\mathbf{z}}$ parallel to the incident field $\mathbf{E}_{inc}$, is given by the Laplace equation in absence of free electric charge:

$$\nabla^2 \phi = 0$$
$$\mathbf{E}_\omega = -\nabla \cdot \phi$$

whose general solution solution, in spherical coordinates, is[5]

$$\phi_{out}(r,\theta) = \sum_{l=0}^{\infty} [\beta_l r^l + \gamma_l^{-(l+1)}] L_l(cos(\theta))$$
$$\phi_{in}(r,\theta) = \sum_{l=0}^{\infty} \eta_l r^l L_l(cos(\theta))$$

with $L_l(cos(\theta))$ the Legendre polynomials. The coefficient β_l,η_l and γ_l are determined by the boundary condition at $z \to \infty$ and by $r = a_0$. If $r \to \infty$ then $\phi = -\mathbf{E}_{inc} r cos(\theta)$ so $\beta_l = 0 \ \ \forall l \neq 1$

and $\beta_1 = -\mathbf{E}_{inc}$. If $r = a_0$ then the normal component of the displacement field must be continuous as well as the tangential component of the electric field. Being so the internal and external potential are just given by

$$\begin{aligned} \phi_{in}(r,\theta) &= -\frac{3\epsilon_m}{\epsilon + 2\epsilon_m} E_{inc} r cos(\theta) = -\frac{3\epsilon_m}{\epsilon + 2\epsilon_m} E_{inc} z \\ \phi_{out}(r,\theta) &= -E_{inc} r cos\theta + \frac{\epsilon - \epsilon_m}{\epsilon + 2\epsilon_m} E_{inc} a_0^3 \frac{cos(\theta)}{r^2} \end{aligned} \tag{2.2.0.8}$$

where E_{inc} is the modulus of the incident field. As consequence, the electric field inside the nanosphere is

$$E_\omega = \frac{3\epsilon_m}{\epsilon + 2\epsilon_m} E_{inc} \hat{\mathbf{z}} \Rightarrow \int_{S_{NS}} |E_\omega|^2 = 4\pi a_0^2 | \frac{3\epsilon_m}{\epsilon + 2\epsilon_m} E_{inc}|^2 \tag{2.2.0.9}$$

Equation 2.2.0.6 can now be used to compute the hot electron distribution per unit of energy:

$$\delta\rho(\epsilon) = \frac{2e^2 E_F^2}{\Gamma \pi^2 \hbar} \frac{1}{(\hbar\omega)^4} 4\pi a_0^2 | \frac{3\epsilon_m}{\epsilon + 2\epsilon_m} E_{inc}|^2 \quad if \quad E_F + \delta E_b < \epsilon < E_F + \hbar\omega \tag{2.2.0.10}$$

where δE_b is determined case by case.

Chapter 3

Methods

3.1 Finite-Difference Time-Domain

Finite Difference Time Domain, from now on FDTD, is a numerical tool based on finite differences to propagate in time and space Maxwell's equations. This method has been designed by Allan Taflove, on the ground of 1966 Kane Yee's paper, to study the effect of electromagnetic devices on the human visual system. Clearly, Maxwell's equations cannot be solved analytically for a complex medium such as the human visual systems therefore a numerical method was imperative to solve the problem. At the beginning, this method has not been much used in the electrical engineering community due to the high cost in terms of computational power and overall memory but in recent days, thanks to the advent of supercomputers and the increase of computational power of common laptop, the DFTD has gained more and more popularity. Indeed, DFTD allows for a precision much higher than other computational method[2].

3.1.1 Finite difference method

The basic idea of 1966 Yee's work is to substitute partial derivatives in Maxwell's equation with finite difference approximation. The finite difference approximation works as follow: let's for instance consider the following two equation

$$f(x+dx) = f(x) + \frac{\partial f}{\partial x}|_x dx + \frac{\partial^2 f}{\partial x^2}|_x dx^2 + \frac{\partial^3 f}{\partial x^3}|_x dx^3 + \frac{\partial^4 f}{\partial x^4}|_x dx^4 + o(x^4) \tag{3.1.1.1}$$

$$f(x-dx) = f(x) - \frac{\partial f}{\partial x}|_x dx + \frac{\partial^2 f}{\partial x^2}|_x dx^2 - \frac{\partial^3 f}{\partial x^3}|_x dx^3 + \frac{\partial^4 f}{\partial x^4}|_x dx^4 + o(x^4) \tag{3.1.1.2}$$

if we subtract 3.1.1.2 from 3.1.1.1 we obtain

$$f(x+dx) - f(x-dx) = 2\frac{\partial f}{\partial x}|_x dx + O(x^4) \tag{3.1.1.3}$$

Let's imagine to take the real line and to divide it equal interval of length dx such that $x = ndx$ so that we can write again the 3.1.1.3 as

$$\frac{f(dx(n+1)) - f(dx(n-1))}{2dx} \simeq \frac{\partial f}{\partial x}|_{ndx} \tag{3.1.1.4}$$

This particular approximation of the partial derivative is called central difference and will be the central tool in DFTD. Even in higher dimension the idea is the same. For instance one can consider a function F of two variable x and y and, following the exact above discussed argument, get

$$\frac{F((n+1)dx, mdy) - F((n-1)dx, mdy)}{2dx} \simeq \frac{\partial F}{\partial x}|_{ndx,mdy}$$
$$\frac{F(ndx, (m+1)dy) - F(ndx, (m-1)dy)}{2dx} \simeq \frac{\partial F}{\partial y}|_{ndx,mdy}$$

To ease the formulas one can use the following ink-saving formalism:
for any given function f, $f(idx, jdy, kdz) \doteq f|_{i,j,k}$. The central difference approximation may as well be applied to derivatives in time. For instance:

$$\frac{\partial E_x}{\partial t}|^n_{i,j,k} \simeq \frac{E_x|^{n+1}_{i,j,k} - E_x|^{n-1}_{i,j,k}}{2dt} + O(dt^2) \tag{3.1.1.5}$$

It is clear that the use of central differences let us having equation accurate up to second order both in time and space.

3.2 Yee algorithm

It is now time to discuss the DFTD method. Firstly, it' s useful to recall Maxwell's equations in an arbitrary media,with no charge density and arbitrary magnetic and electric current source:

$$\begin{aligned} \nabla \cdot \mathbf{D} &= 0 \\ \nabla \cdot \mathbf{B} &= 0 \\ -\nabla \times \mathbf{E} - \sigma^* \mathbf{H} - \mathbf{M}_s &= \frac{\partial \mathbf{B}}{\partial t} \\ \nabla \times \mathbf{H} - \mathbf{J}_s - \sigma \mathbf{E} &= \frac{\partial \mathbf{D}}{\partial dt} \end{aligned} \tag{3.2.0.1}$$

and the constitutive equations:

$$\begin{aligned} \mathbf{D} = \epsilon \mathbf{E} \quad \mathbf{B} = \mu \mathbf{H} \\ \mathbf{M} = \mathbf{M}_s + \sigma^* \mathbf{H} \quad \mathbf{J} = \mathbf{J}_s + \sigma \mathbf{E} \end{aligned} \tag{3.2.0.2}$$

where ϵ is the electric permittivity μ is the magnetic permeability, σ^* is the equivalent magnetic loss and σ is the electric loss. In this treatment only a spatial dependence of ϵ, μ, σ and σ^* is allowed so one can consider only the case when those quantity are scalar. As anticipated,the main idea is to approximate the partial derivatives with central differences. The stroke of genius of Yee consists in the use of a spatial and temporal grid, indeed called Yee grid, that automatically satisfies 3.2.0.1 leaving only the curls equations to be dealt with. This also imply that there is no need to enforce boundary condition in presence of different media since the Yee grid automatically takes care of it [2](3.2.0.1) Applying the finite difference method to Maxwell's equations and using some elementary algebra, one can write down the following six updates equation for the fields components shown in

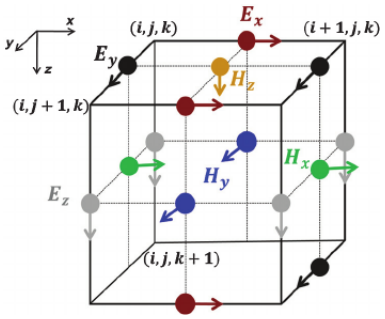

Figure 3.2.0.1: Yee cell. Each electric field component is surrounded by magnetics field components. Intuitively, this grid already satisfies the divergence Maxwell's equations.

figure 3.2.0.1.
Update equations for the electric field components:

$$E_x|^{n+1/2}_{i,j+1/2,k+1/2} = C_1|_{i,j+1/2,k+1/2} E_x|^{n-1/2}_{i,j+1/2,k+1/2} + \\ +C_2|_{i,j+1/2,k+1/2}\left(\frac{H_z|^n_{i,j+1,k+1/2} - H_z|^n_{i,j,k+1/2}}{dy}\right. \\ \left. -\frac{H_y|^n_{i,j+1/2,k+1} - H_y|^n_{i,j+1/2,k}}{dz} + -J_{s,x}|^n_{i,j+1/2,k+1/2}\right) \tag{3.2.0.3}$$

$$E_y|^{n+1/2}_{i-1/2,j+1,k+1/2} = C_1|_{i-1/2,j+1,k+1/2} E_y|^{n-1/2}_{i-1/2,j+1,k+1/2} + \\ +C_2|_{i+1/2,j+1,k+1/2}\left(\frac{H_x|^n_{i-1/2,j+1,k+1} - H_x|^n_{i-1/2,j+1,k}}{dz} - \right. \\ \left. \frac{H_z|^n_{i,j+1,k+1/2} - H_z|^n_{i-1,j+1,k+1/2}}{dx} - J_{s,y}|^n_{i-1/2,j+1,k+1/2}\right) \tag{3.2.0.4}$$

$$E_z|^{n+1/2}_{i-1/2,j+1,k+1} = C_1|_{i-1/2,j+1,k+1} E_z|^{n-1/2}_{i-1/2,j+1,k+1} + \\ +C_2|_{i+1/2,j+1,k+1}\left(\frac{H_y|^n_{i,j+1/2,k+1} - H_y|^n_{i-1/2,j+1/2,k+1}}{dx} - \right. \\ \left. \frac{H_x|^n_{i-1/2,j+1,k+1} - H_x|^n_{i-1/2,j,k+1}}{dy} + -J_{s,z}|^n_{i-1/2,j+1/2,k+1}\right) \tag{3.2.0.5}$$

with the update coefficient defined as:

$$C_1|_{i,j,k} = \frac{2\epsilon|_{i,j,k} - \sigma|_{i,j,k}}{2\epsilon|_{i,j,k} + \sigma|_{i,j,k}}, \qquad C_2|_{i,j,k} = \frac{2dt}{2\epsilon|_{i,j,k} + \sigma|_{i,j,k} dt}$$

Update equation for the magnetic field components:

$$H_x|_{i-1/2,j+1,k+1}^{n+1} = D_1|_{i-1/2,j+1,k+1} H_x|_{i-1/2,j+1,k+1}^{n} + D_2|_{i-1/2,j+1,k+1}\left(\frac{E_y|_{i-1/2,j+1,k+3/2}^{n+1/2} - E_y|_{i-1/2,j+1,k+1/2}^{n+1/2}}{dz} - \frac{E_z|_{i-1/2,j+3/2,k+1}^{n+1/2} - E_z|_{i-1/2,j+1/2,k+1}^{n+1/2}}{dy} - M_{s,x}|_{i-1/2,j+1,k+1}^{n+1/2}\right) \tag{3.2.0.6}$$

$$H_y|_{i,j+1/2,k+1}^{n+1} = D_1|_{i,j+1/2,k+1} H_y|_{i,j+1/2,k+1}^{n} + D_2|_{i,j+1/2,k+1}\left(\frac{E_z|_{i+1/2,j+1/2,k+1}^{n+1/2} - E_z|_{i-1/2,j+1/2,k+1}^{n+1/2}}{dx} - \frac{E_x|_{i,j+1/2,k+3/2}^{n+1/2} - E_x|_{i,j+1/2,k+1/2}^{n+1/2}}{dz} - M_{s,y}|_{i,j+1/2,k+1}^{n+1/2}\right) \tag{3.2.0.7}$$

$$H_z|_{i,j+1,k+1/2}^{n+1} = D_1|_{i,j+1,k+1/2} H_z|_{i,j+1,k+1/2}^{n} + D_2|_{i,j+1,k+1/2}\left(\frac{E_x|_{i+,j+3/2,k+1/2}^{n+1/2} - E_x|_{i,j+1/2,k+1/2}^{n+1/2}}{dy} - \frac{E_y|_{i+1/2,j+1,k+1/2}^{n+1/2} - E_y|_{i-1/2,j+1,k+1/2}^{n+1/2}}{dx} - M_{s,z}|_{i,j+1,k+1/2}^{n+1/2}\right) \tag{3.2.0.8}$$

with the update coefficient defined as:

$$D_1|_{i,j,k} = \frac{2\mu|_{i,j,k} - \sigma|_{i,j,k}^{*}}{2\mu|_{i,j,k} + \sigma|_{i,j,k}^{*}} \quad D_2|_{i,j,k} = \frac{2dt}{2\mu|_{i,j,k} + \sigma|_{i,j,k}^{*} dt}$$

First of all, we must notice that the electric and magnetic field do not exist at the same time step. As we can observe in figure 3.2.0.2, at each time step only one field is updated and the new values are used to updated the other field in the next step. Indeed, the electric and magnetic fields are staggered in time as well as in space to allow the use of central finite difference approximation. Therefore the updates equations allow us to compute the future values of the electric field and of the magnetic field just by knowing the present fields values. Hence it is possible to appreciate the power and simplicity of the FDTD method.

3.3 Numerical stability of FDTD algorithm

The basic procedure for the analysis of the stability of the algorithm involves the injection of a plane wave $\mathbf{E} = \mathbf{E}_0 e^{(i\omega n dt - i\mathbf{k'}\cdot\mathbf{x})}$ with $\mathbf{k'} = (k_x, k_y, k_z)$ a numerical wavevector into the FDTD equations. After some algebraic manipulation finally one get the numerical dispersion relation[2]:

$$[\frac{1}{cdt} sin(\frac{\omega dt}{2})]^2 = [\frac{1}{dx} sin(\frac{k_x dx}{2})]^2 + [\frac{1}{dy} sin(\frac{k_y dy}{2})]^2 + [\frac{1}{dz} sin(\frac{k_z dz}{2})]^2. \tag{3.3.0.1}$$

Comparing 3.3.0.1 with the ideal dispersion relation for a plane wave $(\frac{\omega}{c})^2 = k_x^2 + k_y^2 + k_z^2$, it's possible to notice that a numerical plane wave feels the Yee grid as an anisotropic medium. This

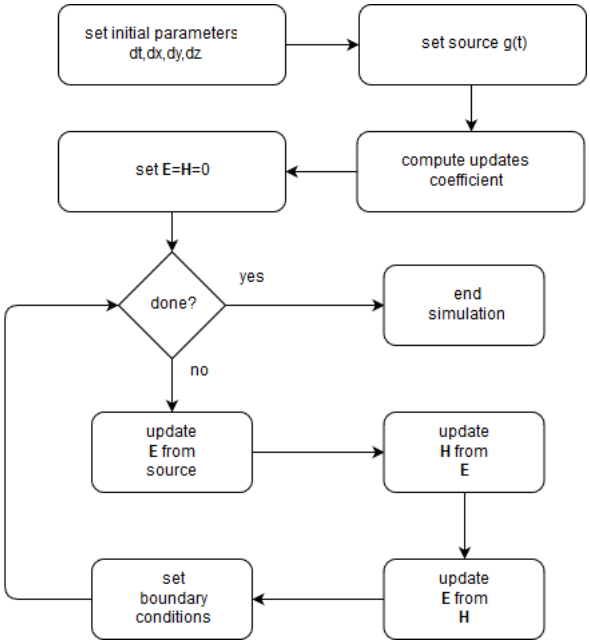

Figure 3.2.0.2: FDTD flowchart

explains the so called numerical dispersion: a plane wave will have a different numerical phase velocity depending on the direction. In general, as dt, dx, dy and dz tends to zero,the numerical dispersion relation tends to the ideal dispersion relation. This may suggest that using a finer grid could reduce the numerical dispersion. Equation 3.3.0.1 shows also another possible problem: the possibility of having a complex ω. Indeed, if a bad choice of dt or a bad design of the Yee cell lead to a complex ω and its imaginary part happen to be negative, then the solution would diverge in time giving rise to a numerical instability of the solution. A good prescription is $S = cdt/dx_{min}/ < 1$, where S is known as the Courant factor and $N_\lambda = \lambda_{min}/dx >> 2$with λ_{min} the smallest wavelenght the user wants to correctly simulate. A realistic value of N_λ is around 20 while a rule of thumb for S is 0.5.

3.4 Boundary condition: UPML

As in every numerical algorithm, numerical boundaries conditions needs to be carefully taken care of. The most simple choice of numerical boundary condition would be to use some fixed boundary condition, for example requiring a zero value for all the field on the boundary of the grid. However, these boundary condition, known as Dirichlet boundary conditions, would behave just like mirrors for the electromagnetic field. As result, the system would be full of spurious electromagnetic waves generated by the boundary condition and the results completely unreliable. What is ideally required should be to have the electromagnetic field freely propagate through the boundary of the numerical grid, without having to worry about reflected waves. This result can actually be obtained by mean

of the uniaxially perfectly matched layer, from now on called UPML. The basic idea, in this case, is to cover the volume where the simulation takes place with an ideal material that does not reflect any waves and, instead, adsorb them. This ideal material is therefore called uniaxially perfectly matched layer. It's numerical formulation can be obtained firstly considering the case of a wave propagating through an infinite interface set in z=0. The dielectric permittivity and magnetic permeability are assumed to be an arbitrarily scalar constant in the $x < 0$ and must be determined in $x > 0$ to have a fully transmitted wave, without any reflection effect. For convenience the medium in $x > 0$ is assumed to be uniaxial, namely

$$\bar{\epsilon}_2 = \epsilon_2 \begin{bmatrix} a & 0 & 0 \\ 0 & b & 0 \\ 0 & 0 & b \end{bmatrix}, \quad \bar{\mu}_2 = \mu_2 \begin{bmatrix} c & 0 & 0 \\ 0 & d & 0 \\ 0 & 0 & d \end{bmatrix}$$

Let's assume the electromagnetic field in $x < 0$ is a plane wave of the form $\mathbf{H}_1(\mathbf{r}) = \mathbf{H}_1 e^{-jk_{1_x}x - jk_{1_y}y}$. Imposing the Maxwell's curl equation in x=0, one can derive the dispersion equation for the electromagnetic field in $x > 0$:

$$\mathbf{k}_2 \times \mathbf{E}_2 = \omega\bar{\mu}_2\mathbf{H}_2 \quad \mathbf{k}_2 \times \mathbf{H}_2 = -\omega\bar{\epsilon}_2\mathbf{E} \Rightarrow$$
$$\Rightarrow \mathbf{k}_2 \times (\epsilon_2^{-1}\mathbf{k}_2) \times \mathbf{H}_2 + \omega^2\bar{\mu}_2\mathbf{H}_2$$

Equation 3.4.0.1 can be solved giving as result four eigenmodes divided into forward and backward TM and TE modes. As result[2]

$$k_{2_x} = (k_2^2 bd^{-1} - k_{1_y}a^{-1}b)^{1/2}, \qquad k_{1_y} = k_{2_y}$$

Then, the reflection coefficient $\Gamma = \frac{E_{reflected}}{E_{incident}}$ and the transmission coefficient $\tau = \frac{E_{transmitted}}{E_{incindent}}$ reads:

$$\Gamma = \frac{k_{1_x} - k_{2_x}b^{-1}}{\beta_{1_x} + \beta_{2_x}b^{-1}}, \qquad \tau = 1 + \Gamma = \frac{2k_{1_x}}{k_{1_x+k_{2_x}}b^{-1}}$$

Hence, in order to set Γ to zero it is sufficient to put $\epsilon_1 = \epsilon_2, \mu_1 = \mu_2, d = b = a^{-1}$. Combining all those choices into one single result leads to the actual dielectric permittivity and magnetic permeability tensor

$$\begin{aligned} \bar{\epsilon}_2 &= \epsilon_1\bar{\nu}_x \qquad \bar{\mu}_2 = \mu_1\bar{\nu}_x \\ \bar{\nu}_x &= \begin{bmatrix} \nu_x^{-1} & 0 & 0 \\ 0 & \nu_x & 0 \\ 0 & 0 & \nu_x \end{bmatrix} \end{aligned} \tag{3.4.0.1}$$

Equation 3.4.0.1 is valid for any arbitrary ν and is totally independent from the angle of incidence of the incident wave. The whole reasoning can be repeated for a wave propagating in any direction. The higher dimensionality generalization of UPML boundary condition is therefore straightforward: for a 3D case[2]

$$\bar{\nu} = \bar{\nu}_x\bar{\nu}_y\bar{\nu}_z$$
$$\nu_\alpha = \kappa_\alpha - \frac{j\sigma_\alpha}{\epsilon_1\omega}$$

Lately, the choice of σ_α and κ_α is done case by case, in order to obtain the desired attenuation of the intensity of the field and no dispersion.

3.5 FDTD software: NANOCPP

Maxwell's equation can be solved analitically only for few ideal nanoparticle's geometry hence, to study how their shape and geometry affect their hot electrons generation rates, is necessary to use a numerical approach. The exploited numerical approach is the finite-difference time-domain method which allows to propagate Maxwell's equation in time on a given space domain with high accuracy. To do so, NANOCPP, an FDTD software optimized for massive parallel computing and developed by professor Fratalocchi's team, is used. NANOCPP takes the following input: a volume where the simulation is done, the number of unitary Yee cell per side of it that automatically determines the resolution of the algorithm, the geometry of the system under investigation, the electromagnetic source and the boundary condition. NANOCPP produces a variety of binary files as output. For the cases of interest, the output produced are the electric field and the electromagnetic energy computed over the whole Yee grid filling the simulation volume and occasionally an electric or magnetic field in time at a specific point in the simulation space.

Chapter 4

Results

4.1 Simulations procedure and data analysis for single particles

The computation for a gold nanoparticle of radius 34.54 nm in air is now discussed in detail in order to show the simulation and data analysis procedure for the single particles hot electron generation rates.
In any simulation both air and gold are treated as dispersive material, even if at optical frequencies both show minimal dispersive properties. The nanospheres is studied under an incident plane wave whose wavelength ranges from 300 nm to 800 nm in steps of 5 nm covering the whole visible spectrum. The resolution of the grid is 1 nm and the number of unitary cell per box side is 200 allowing more than 20 points per diameter of the smallest sphere. Regarding the boundary condition, an UPLM layer of 25 nm width is used. A graphical example of this system is shown in figure 4.1.0.1. The time step is automatically computed by NANOCPP enforcing the Courant stability criterion and in this case is 9.62917×10^{-19}s. The system should be in steady state so the number of time steps must be large enough to allow to any transient dynamic to extinguish. Actually, it is enough to wait for few optical cycle of the incident plane wave so the number of time step of every simulation is set to be equivalent to six optical cycles. The first five are used to let any transient extinguish and then, during the sixth, the electric field is recorded every hundred time step. These sample will be used to compute the average of the modulus square of the electric field over an optical cycle as

$$\left\langle |E_{\omega,n}(\mathbf{r})|^2 \right\rangle = \frac{1}{N_\omega \Delta t} \sum_i |E^{(i)}_{\omega,n}(\mathbf{r})|^2 \Delta t, \quad 1 < i < N_\omega \tag{4.1.0.1}$$

with N_ω the number of sample of the electric field taken during an optical cycle. The main object to be numerically computed is the normal to the surface electric field $\mathbf{E}_{\omega,n}$. At the end of the computation, NANOCPP produces a binary file for each component of the electric field. Once those files are properly reshaped, the electric field components are written as three dimensional array E_x, E_y, E_z such that $E_\alpha[i,j,k],\ \alpha \in x,y,z$, is the α component of the electric field evaluated at the [i,j,k] cell. The first issue to be resolved is finding all the point belonging to the surface of the sphere. To do so, first a change of coordinates that moves the origin of the system, located in

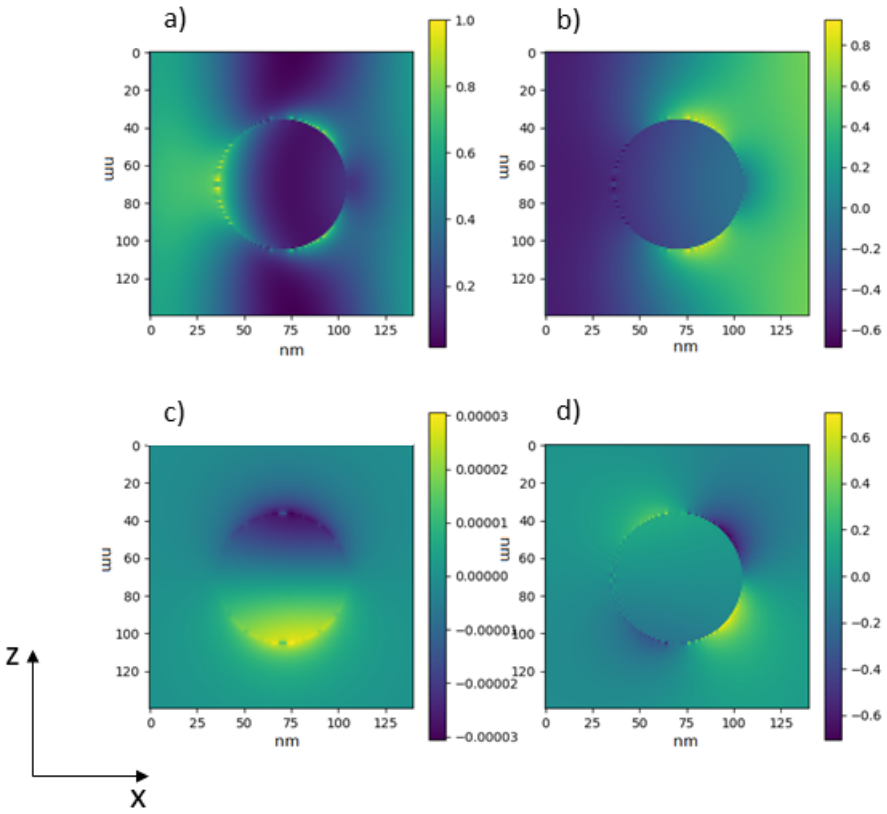

Figure 4.1.0.1:
simulation of a gold nanosphere of radius=34.54 nm excited by a monochromatic plane wave of wavelength=300nm. It is clear the dipole-like beahaviour which characterizes the energy and field distribution;
a) electromagnetic energy distribution in the (x,y=100nm, z) plane, arbitrary units;
b) $E_x(x = 100nm, y = 100nm, z)$, arbitrary units;
c) $E_y(x, y = 100nm, z = 100nm)$, arbitrary units;
d)$E_z(x, y = 100nm, z)$, arbitrary units;

lower left corner of the air box, to the center of the sphere has been exploited. Clearly, the point laying on the surface of the sphere are such that their distance from the center of the sphere, now in (0,0,0), is equal to the radius. Due to the discrete character of the Yee grid, just searching for the those points would produce no output. Therefore a nearest neighbour strategy has been involved to find all the points laying on the surface of the nanoparticle. This is possible because NANOCPP creates a geometry file such that the points belonging to the nanostructure have a value different from the zero value assigned to points belonging to the surrounding air. Therefore, it is enough to look for the set of points [i,j,k] such that:

$$f[i,j,k] \neq 1 \quad and \quad \exists f[l,m,n] = 1,\ [l,m,n] \subset NN[i,j,k]$$

where NN stands for nearest neighbours. It is worth to notice that this approach to find the surface points is effective regardless of the shapes, so it is completely general. Once this is done, the next step consist in computing normal to the sphere surface component of the electric field. First the normal to the surface versor is computed considering the vector joining the desired surface point with the origin and dividing its components by its modulus. The normal electric field is finally computed projecting the total electric field on the normal versor at each point of the surface. After computing its time-average as shown in equation 4.1.0.1, one can compute the power spectral density $S(\omega)$ defined as

$$S(\omega) = \int_{S_{NS}} \frac{\left\langle |E_{\omega,n}|^2 \right\rangle}{(\hbar\omega)^4} \tag{4.1.0.2}$$

which can be numerically computed , at each frequency, as

$$\int_{S_{NS}} \frac{\left\langle |E_{\omega,n}|^2 \right\rangle}{(\hbar\omega)^4} \approx \sum_{[i,j,k]\in S_{NS}} \Delta s \frac{\left\langle |E_{\omega,n}[i,j,k]|^2 \right\rangle}{(\hbar\omega)^4}$$

where Δs is a single face unitary Yee cell surface, in this case equal to $10^{-18} nm^2$, and the total mean normal field under a broadband optical source $E_n^t(\mathbf{r})$ defined as

$$I(\mathbf{r}) = \int_{\lambda=300nm}^{\lambda=800nm} \left\langle |E_{\omega(\lambda),n}(\mathbf{r})|^2 \right\rangle d\omega \tag{4.1.0.3}$$

which can be numerically computed as

$$\int_{\lambda=300nm}^{\lambda=800nm} \left\langle |E_{\omega(\lambda),n}(\mathbf{r})|^2 \right\rangle d\omega \approx \sum_{\lambda_i\in[300nm,800nm]} \left\langle |E_{\omega(\lambda_i),n}[i,j,k]|^2 \right\rangle \Delta\omega \tag{4.1.0.4}$$

where [i,j,k] are such that $\mathbf{r} \approx [i\Delta x, j\Delta y, k\Delta z]$. $I($**r** is useful to visualize how the rate of generation of hot electron varies on the nanostructure's surface. The whole procedure used for the computation of $I(\omega)$, which is a photonic surface density of states, $S(\omega)$ and $I(\mathbf{r})$, except for the computation of the normal versor to the surface which is anyway trivial for standard geometries, is totally general and is used to compute the relevant quantity for all the single particle shapes considered.

4.2 Hot electron generation rate for single particle shapes

As shown in the previous sections, the hot electron generation rates strongly depends on the nanoparticles shape. The set of shapes considered includes the sphere, the ellipsoid, the nanocube and the cylinder. All the shapes have been designed such that all have a surface area equal to the one of a 25nm side cube. These geometries have been chosen because these are the most simple to experimentally realize with a good control of shapes and position of the nanoparticles. The first shape here considered is the spherical one. The simulations shows that the sphere practically behave like a dipole, in good agreement with the quasi static model[5]. Indeed, as it is shown in figure 4.2.0.1, the electromagnetic field reaches its greater intensity at the poles of the sphere in the z direction, which is actually the wavelength direction of the exciting field. Of greater interest are the power spectral density $S(\omega)$ and the total mean normal field E_n^t. As shown in the top left of

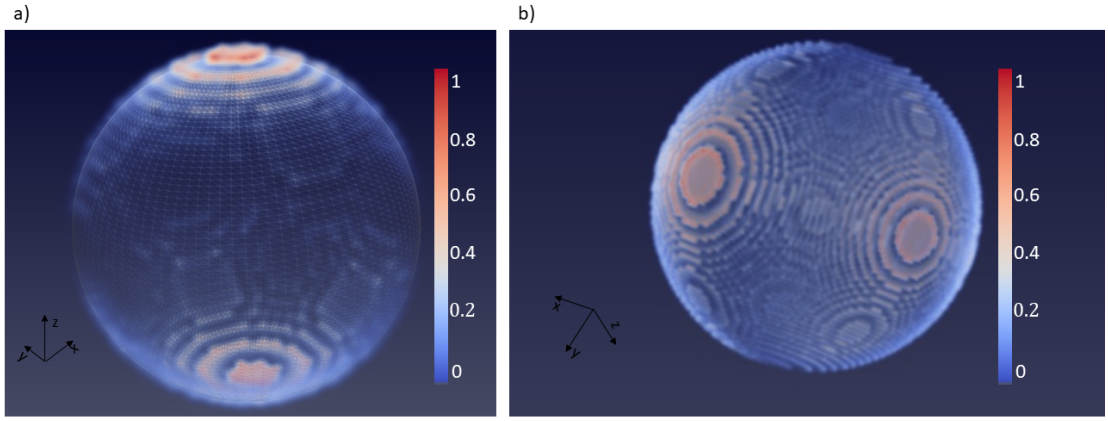

Figure 4.2.0.1:
a) 3D photonic surface density of states for a sphere of diameter equal to 34.54 nm excited by a monochromatic field of 300 nm wavelength, arbitrary units;
b) hot electron generation rate in space, arbitrary units.
In both images the dipole behaviour is clearly evident, as well as the enhancement of the electric field at the two poles of the sphere. However, some interference's patterns are visible on the rest of the surface of the sphere.

figure 4.2.0.2 , $I(\omega) = \int_{S_{NS}} < |E_{\omega,n}|^2 >$ shows a peak which is fairly close to the one exhibited by the power spectrum of the electric field on top of the sphere, shown in the right side of figure 4.2.0.2. The power spectrum peak's frequency coincides with the resonant modes of the sphere so $I(\omega)$'s frequency peak is due to the nanosphere's resonant modes. Nevertheless $S(\omega)$, shown in the left bottom of figure 4.2.0.2, exhibits a quite broadband behaviour particularly in the near infrared and low optical frequency region. The nanosphere's hot carrier generation rate will therefore increase as the frequency of the incident light decreases. Nonetheless, it shows a broadband behaviour in the visible light spectrum. Finally, the bottom part of figure 4.2.0.1 shows the space distribution of the total time-averaged modulus square of the normal electric field. It is clear that the only a small portion of the surface, located in the poles of the sphere, contributes incisively to the hot electron generation rate and this portion coincides with the high intensity field due to the dipole-like behaviour of the sphere.

The second geometry considered is the elliptical one. The main feature of the ellipsoid is that the resonant peak of the nanoparticle is red shifted with respect to the sphere's one. This actually means that the ellipsoid exhibits a less broadband hot electron generation rate since the enhancing effect of $(\hbar\omega)^{-4}$ is not able to increase the peak amplitude of the integrated normal field intensity, as shown in the bottom left image of figure 4.2.0.3. As well as in the sphere case, the peak of both

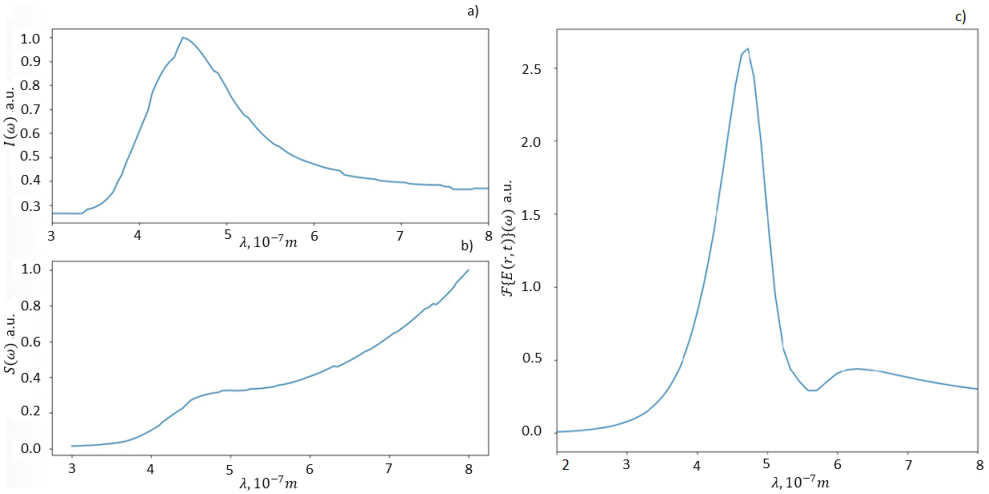

Figure 4.2.0.2:
a) $I(\omega)$ of a 34.54 radius gold nanosphere, arbitrary units;
b) $S(\omega)$ for the same gold nanosphere, arbitrary units;
c) $|\mathcal{F}\{E\}|^2$ in the north pole of the sphere, namely where the field reaches its maximum intensity, arbitrary units

$I(\omega)$ and $S(\omega)$ coincide with the resonant mode frequency ellipsoid, as shown in the top left of figure 4.2.0.3. Also in this case the electric field reaches its maximum intensity at the poles of the nanoparticles, hence exhibiting an even more clear dipole-like behaviour with respect to the sphere showed in figure 4.2.0.3. This behaviour is well explained by the tip effect of the electromagnetic field: the greater the radius of curvature of the object, the greater the intensity of the electric field of the tip. Here the ellipsoid doesn't have a real tip but the radius of curvature increases considerably at the two poles, where the field reaches its maximum intensity.

The third geometry analyzed is the the cubic one and, as in the previous case, the material chosen is gold. As can be seen from the top left image of figure 4.2.0.4, the cuboid resonant frequency, which is around 500 nm, is in the ideal position to give rise to a broad hot electron generation rate. Indeed, as shown in the bottom left plot of figure 4.2.0.4 the hot electron generation rate of the cuboid is really wide and has a great contribution also from the infrared frequency. The enhancement of the electric field is greater on the cuboid than on the other geometries due to the corners. Indeed, as shown in the right image of figure 4.2.0.4, the electromagnetic field reaches an intensity on the corner of the cube of one or even two order of magnitude greater than the normal field on the rest of the surface. As in the previous case, this enhancement of the electromagnetic field on the surface of the nanocube is due to the tip effect, which is greatly increased by the presence of proper tips[12].
The last geometry investigated is the cylindrical one. The cylindrical geometry has significant relevance because, as the sphere, is one of the most simple structure that can be nanofabricated.

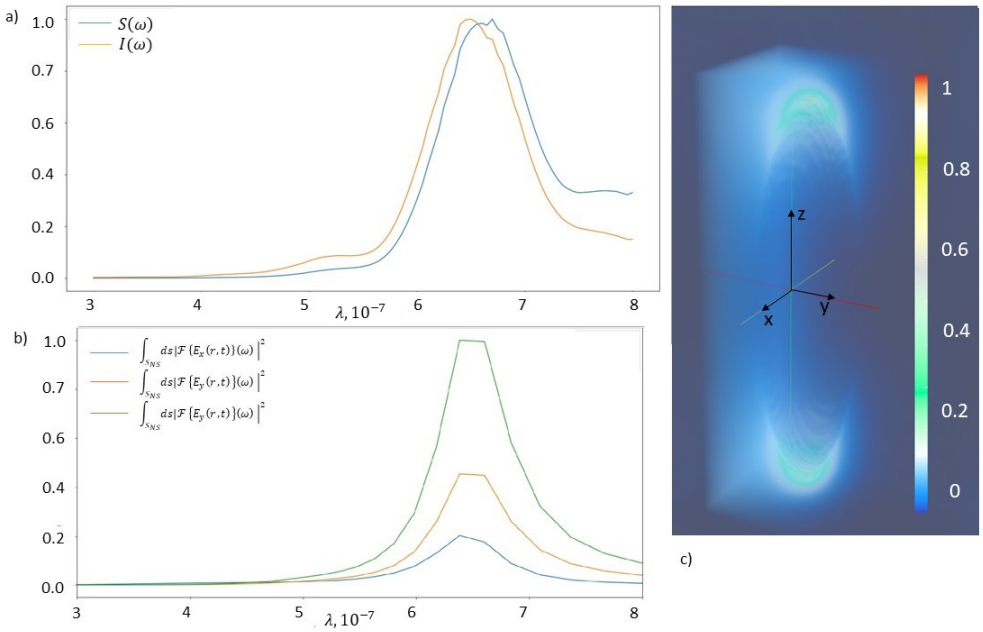

Figure 4.2.0.3:
a) $I(\omega)$ and $S(\omega)$ for the ellipsoid normalized respectively to their maximum value;
b) the density of photonic states of the ellipsoid for each component of the electric field, arbitrary units. The total density of photonic states is given by the sum of the three contributes;
c) local photonic density of states integrated over the surface of the ellipsoid integrated over the wavelength range of the visible light, arbitrary units.

Indeed, the electron beam litography allows to fabricate this shapes with high control on the geometrical features. As can be observed in the top left of figure 4.2.0.5 , the cylinder has his peak at 500nm, quite close to the one of the sphere, but it has a much broader behaviour than it. This is reflected also in his hot electron generation rate behaviour in frequency that follows quite closely the one of the sphere. However the cylinder presents a discontinuity in the geometries that enhances the electromagnetic field on the borders of the two faces, as can be observed in the right image in figure 4.2.0.5.
In conclusion, it is possible to observe that, among the various elementary gold nanoparticles, the most promising one in terms of broad behaviour in the visible electromagnetic spectrum is the cubic one. Indeed its peak position is ideal to obtain a broad hot electron generation rate which is certainly also due to the presence of the hot spots. Since, anyway, this kind of shapes is quite hard to obtain, another good option is the cylindrical one. Even if it does not presents an intensity spectrum as broad as the cubic one, it is as broad as the spherical one but also of much simpler realization than it . As already pointed out, the use of the electron beam litography would allow the precise control of the size as well as position of the nanopillar, which will be shown later to be of extreme importance when dealing with arrays of nanoparticles.

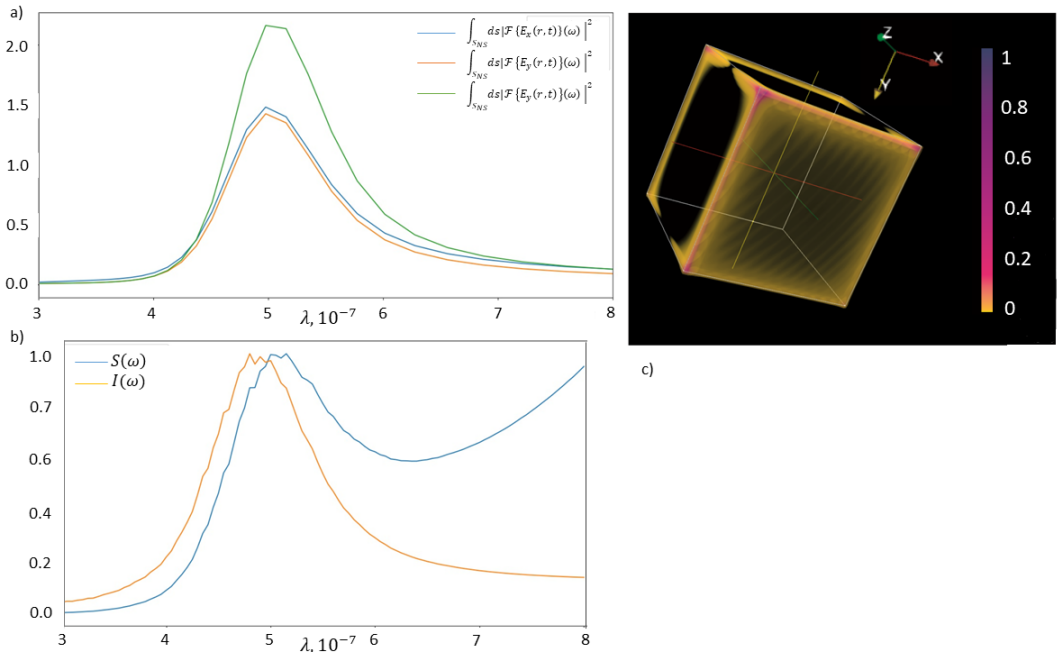

Figure 4.2.0.4:
a) I(ω) and $S(\omega)$ normalized to their respective values for the cuboid fo side length equal to 25 nm; b) the three components of the integrated in space photonic DOS, arbitrary units. The total DOS is simply obtained by their sum. The peak of the DOS and of the electric field intensity is fairly equal, hence also in the cuboid case the electric behaviour is dominated by the plasmonic resonances. However, the hot electron generation rate is quite broad in frequency due to the excellent position of the peak frequency and to the term $(\hbar\omega)^{-4}$;
c) $I(\mathbf{r}) = \int_{visible\ spectrum} d\omega \langle |E_{n,\omega}(\mathbf{r})|^2 \rangle$, arbitrary units. It is clear how the presence of the corners increases the enhancement of the field. This is in agreement with what found by Govorov and collaborator, which they refers to as hot spot[12].

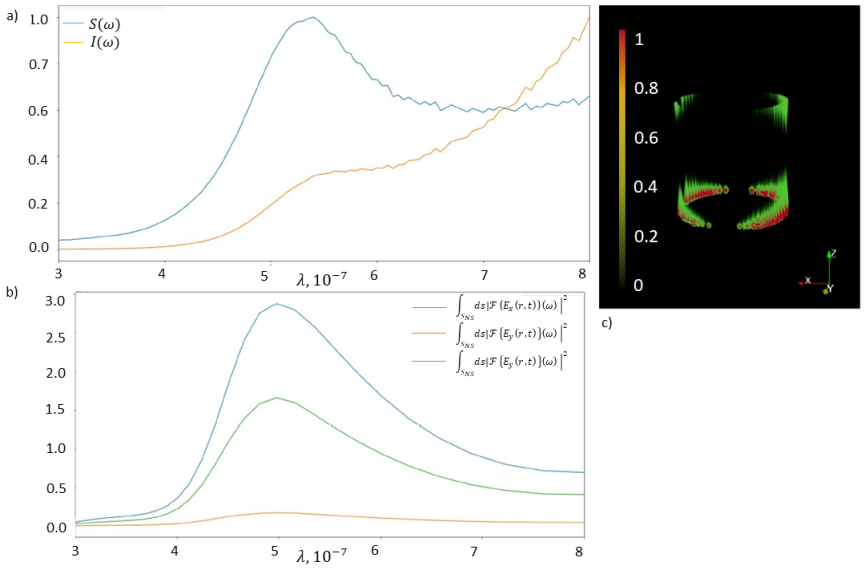

Figure 4.2.0.5:
a) I(ω) and $S(\omega)$ normalized respectively to their maximum value;
b) the three components of the photonic DOS integrated in space in arbitrary units. The total DOS is simply obtained by their sum. The peak of the DOS and of the electric field intensity is fairly equal, hence also in the cylinder case the electric behaviour is dominated by the plasmonic resonances. The hot electron generation rate is as broad in frequency as the sphere thank to the good position of the peak frequency. Anyway it is still less broad than the cuboid case;
c) $I(\mathbf{r}) = \int_{visible\ spectrum} d\omega \langle |E_{n,\omega}(\mathbf{r})|^2 \rangle$, arbitrary units. The presence of the discontinuities in the geometry leads to a greater enhancement and localization of the electric field on the surface of the structure. Also in this case, the intensity of the electric field is expressed in arbitrary units.

4.3 Hot electron generation rate for disordered arrays of nanoparticles

It is clear that the properties of a single particle, as promising as they may be, are of limited interest when it come to a massive generation of hydrogen. Indeed, in order to reach an hydrogen production per unity of surface as a great as possible, it is mandatory the use of highly packed arrays of nanoparticles. Anyway, in the contest of the Coupled Mode Theory, from now on CMT[3], it is well known that ordered arrays of nanoparticles behaves just like coupled arrays of open cavities. In the CMT, each particles is reduced to a hertzian dipole $p_{i,m}$, where i stands for the polarization and m stands for the position of the dipole in the array, which has is own resonance frequency and which interacts , at least as a first approximation, with its nearest neighbours. Hence, each particle is well described by

$$-\omega^2 p_{i,m} = -\omega_0 p_{i,m} - i\Gamma_r \omega p_{i,m} - i\frac{\Gamma_{ff}}{\omega_0}\omega^3 p_{i,m} - \gamma i\omega_c^2(p_{i,m-1} + p_{i,m+1}) \tag{4.3.0.1}$$

where Γ_r is the relaxation constant due to electron-electron, electron-phonon and electron-defects interaction and is given by the Matthiessen rule, ω_0 is the single particle resonance frequency, Γ_{ff} is the relaxation constant due to the far field emission, γ_i an O(1) polarization dependent term and ω_c a coupling constant among nearest neighbours dipoles. Clearly this set of coupled equation is actually similar to the one describing the ion motion in a lattice[6] therefore, as well as ions in a solid lattice, they will behave collectively and will oscillate at highly localized frequency in the visible spectrum. This implies that, regardless to the single particle's spectrum, much of the incident wavelength would be wasted. In order to extract as much energy as possible from the solar energy, the array must have a broad hot electron generation rate spectrum hence should be able to generate plasmonic resonances over a large set of frequency. Therefore the following questions rise spontaneously: is it possible to break down this collective behaviour and obtain a spectrum which is somehow the sum of many different single cavities spectrum? If the answer is positive, which strategy would allow to do that?

To answer to these question one should understand the root of this collective behaviour, which lies in the symmetries and constants of the systems. As just said, the array of nanoparticles is, physically speaking, nothing more than an set of coupled oscillators subjected to a forcing field, which is the monochromatic external field, and to a dissipation process. As long as the constants of the system, namely the center to center distance and the shape of the single constituent, and its symmetries are conserved the array will only oscillates at few deterministic frequencies. It is only natural to think that, to break down the collective behaviour, one should break the symmetries and constants of the system.

As already noticed, the CMT involves directly the resonance frequency of the single particle, which is a function of the shape and size of it, the relaxation constant, which are function of size and shape of the constituents as well as of their relative distance, and the coupling coefficient which goes as $\frac{1}{d^3}$ and which explain why only nearest neighbours are taken into account. The break of any of the constants or symmetries would affect deeply the system so the ensemble of possible scenarios is too large to be fully explored. In this framework the paper of of Gongora and Fratalocchi[10] is a good starting point.

In their paper, they have shown how the introduction of disorder in a 1D array of metal nanoparticles can lead to an extremely localized field on the surface of the nanoparticles, which in turn leads, in the frequency space, to an high enhancement of the fields and to a broad spectrum. To show that,

the theory of the product of random matrix, from now on PRM[1], has been used to describe the nanoparticles array. Each cavity can indeed be described by a matrix M_n and the whole system is the product of the matrices describing each cavity $P_N = \prod_{i=1}^{N} M_n$. If no disorder is allowed in the system, the study of the eigenvalues of P_N leads to the resonance frequency of travelling plasmonic waves as well as to their characteristic decaying time[3]. However, when a random degree of freedom is introduced into the system the way to deal with it changes radically. Let's consider for instance one of the simplest case of disordered arrays, the binary one. In a binary disordered array each particle, which will be assimilated to a sphere, can be of type A or B, the type A being characterized by a radius equal to 25nm and the type B being characterized by a radius of 20nm while the center to center distance is kept fixed. The total number of particle N is fixed, as well as the number of particle of type A, $N_A = pN$, and of type B, $N_B = N - N_A$, with $p \in [0, 1]$. The ensemble of all possible realization of this array, called microcanonical in analogy with the microcanonical ensemble in statistical mechanics, is obtained through a random shuffle of the particles in the array such that all the realization at fixed p are equally probables. Again, the system is described by the product of all the matrices which are themselves random quantities. The properties of the system are then given by the characteristic Lyapunov exponent[1], from now on CLE, γ_l defined as:

$$\gamma_l = log(\langle Tr[\prod_{i=1}^{N} T_n] \rangle_m) \tag{4.3.0.2}$$

where $\langle ... \rangle_m$ mean the average over the microcanonical realizations ensemble. The inverse of the real part of the CLE is the localization length of the array and is proportional to the inverse of the electromagnetic normalized participation ratio

$$\Re\{\gamma_l^{-1}\} \approx \langle l_c \rangle_m = \langle \frac{(\int_V \mathcal{E})^2}{V \int_V \mathcal{E}^2} \rangle_m \tag{4.3.0.3}$$

In the 1D case, using this approach, they have shown how $\Re\{\gamma_l\}$ has a well defined minimum as function of p corresponding to the minimum of the participation ratio itself computed using the FDTD. One can therefore expect that the hot electron generation rate may actually benefit from this kind of disorder if, in the 2D case, the same kind of disorder would lead to a broadband spectrum and to an increased enhancement of the electromagnetic field at the nanoscale. These have been the reasons for the choice of the binary and ternary, in which each particle can have three different radii, 2D arrays of nanopillars. The choice of the nanopillars as single particle shape is due to their performance, their simplicity of fabrication, which makes them good candidates for a real experiment, and to the smaller amount of time need to simulate them with respect to the other shapes. Indeed, if their height is large enough, a 2D FDTD set of simulation can be used instead of a 3D one.
Nevertheless, the fabrication of such a system would be pretty challenging since it would need an insane control of position and shapes of the nanoparticle. As any real process, it is subject to some errors which will always prevent the realization of any structure with absolute precision, so one may think of using these fabrication limits to its own advantage. This is basically the reason to study arrays in which the radius of the nanopillars is fixed and their position, along one or both the direction, is a random variable with a gaussian distribution.

4.3.1 2d arrays geometrical features and simualtions details

The study of a 2d array of nanopillars presents a great theoretical challenge already at the beginning. Indeed, despite in the 1d case the product of random matrices could be done only from the source to the last of the cavities, in the 2d case there is a new degree of freedom that makes everything more complicated and it is the order of the product. In general, the product of matrices is not commutative, therefore not all the product order are equivalent. Unluckily, there is no clue about which order one should use, therefore only the study by mean of numerical simulation is reliable. Hence, the only resource at disposal is the numerical computation of the localization length for the various systems.
To compute the localization length, a set of massively parallel 2D FDTD simulations on Shaheen, KAUST's supercomputer, has been used. The fundamental features of the FDTD simulation are identical for the four system considered. The simulation domain is a 1.825 nm times 1.825 nm square with a resolution of 1 nm, enough to have more than 100 elementary cells in the the length of the shortest wavelength, which is 300 nm. A 60 cells layer of UPML has been used for the boundary condition, and the TFSF box has been set such that it goes from 60 nm to 1.765 μm along the x and y directions. The number of pillar is set to 400, 20 along the x directions and 20 along the y direction. The nanopillars material is gold while the background material is air and both are treated as dispersive material, to obtain results as close to the reality as possible. The integration domain of the localization length instead starts at 100 nm and ends at 1.75 μm on each side. Each system is different since it exhibits a different kind of disorder and randomness therefore

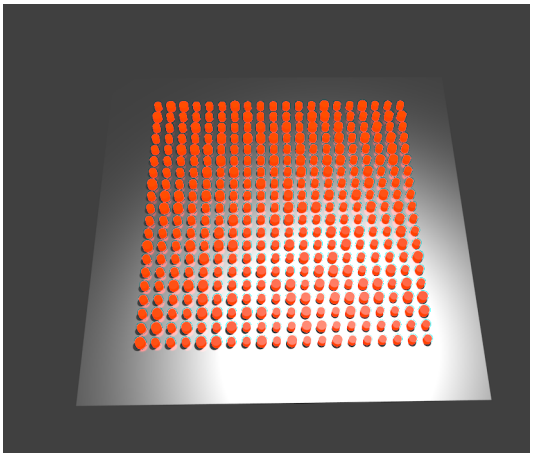

Figure 4.3.1.1: a)

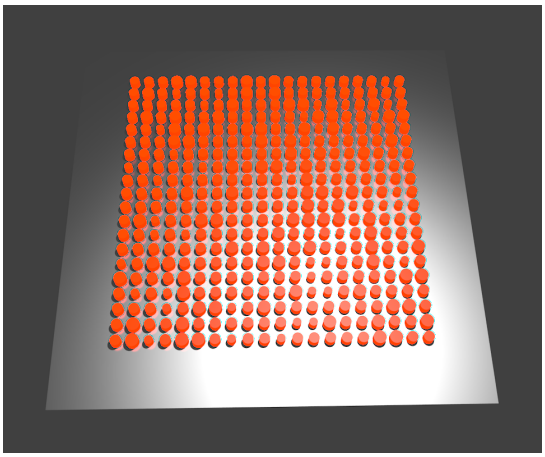

Figure 4.3.1.2: b)

Figure 4.3.1.3:
a) 2d binary array realization with p=0.68;
b) 2d ternary array realization with $p_1 = 0.68,\ p_2 = 0.1$.

for any of them a different algorithm has been used to generate their realization. In the binary case, the center to center distance is kept fixed, as shown in figure 4.3.1.1 while the radius of the particle changes in such a way that, given the total number of particles N, the number of particle of radius equal to 20 nm is int(pN) and the number of particle of radius equal to 25 nm is int($(1-p)N$). To

obtain such a realization of the 2d binary array is then enough to take a 1d array of length N in which the first int(pN) elements are set equal to 20 nm and the rest are set equal to 25 nm. The last step is to randomly shuffle and reshape it in the form of a 20 times 20 array. This algorithm ensures that all the realization at fixed p and N are, indeed, equally probables. The case of the 2d ternary array, a realization of which is in figure 4.3.1.2, is pretty much the same as the 2d binary array, but it is characterized by two parameters: p_1 and p_2. In this system, each particle's radius can be equal to 20 nm, 25 nm or 30 nm and, just like for the 2d binary array, the center to center distance in kept fixed to 75 nm so, at fixed p_1 and p_2, the number of particles of radius equal to 20 nm is $p_1 N$, the number of particle of radius equal to 25 nm is $p_2 N$ and the number of particles of radius equal to 30 nm is $(1 - p_1 - p_2)N$.

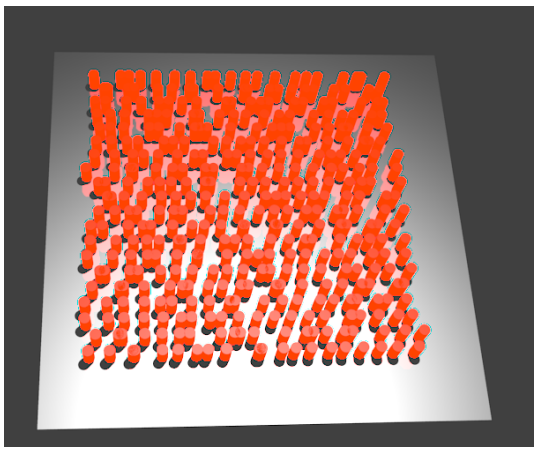

Figure 4.3.1.4: a)

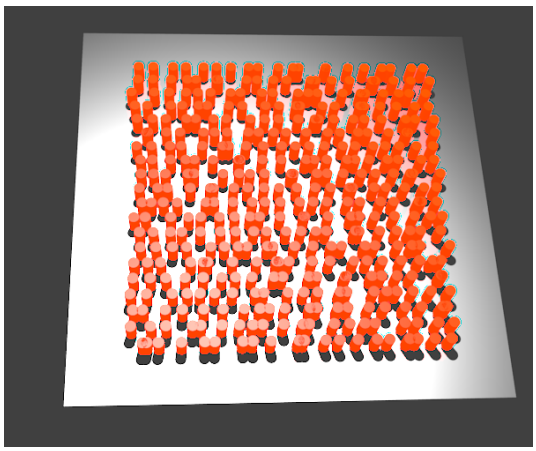

Figure 4.3.1.5: b)

Figure 4.3.1.6:
a) 2d gaussian x array realization with $\sigma = 24nm$;
b) 2d gaussian xy array realization with $\sigma = 22nm$.

4.3.2 Localization length

The localization length, which is indeed given by the participation ratio, is a first measure of the enhancement of the electromagnetic field induced by the different geometries. The localization length is defined as[10]

$$\langle l_c \rangle_m = \langle \frac{(\int_V \mathcal{E})^2}{V \int_V \mathcal{E}^2} \rangle_m \tag{4.3.2.1}$$

The algorithm to generate equally probables realization at fixed p_1 and p_2 is almost identical to the binary array's one, the only difference being in the initialization of the 1d initial array in which int($p_1 N$) elements are set to 20 nm, int($p_2 N$) are set to 25 nm and the rest is set to 30 nm. For the gaussian x and gaussian xy array, the procedure is slightly different. Indeed, here it is the radius of the particles to be kept fixed and their position to be generated according to a probability distribution. The starting point is a 2d array of perfectly equally spaced particles of 25 nm radius

such that their center to center distance is equal to 75 nm. Then, each particle position is perturbed according to a normal distribution as shown in equation 4.3.2.2

$$\begin{gathered}\mathbf{r}_{i,j} = \bar{\mathbf{r}}_{i,j} + \delta\mathbf{r} \\ \delta\mathbf{r}_x \sim \mathcal{N}(0,\sigma),\ \delta\mathbf{r}_y = 0 \quad for\ the\ gaussianx\ case \\ \delta\mathbf{r}_x \sim \mathcal{N}(0,\sigma),\ \delta\mathbf{r}_y \sim \mathcal{N}(0,\sigma) \quad for\ the\ gaussian\ xy\ case.\end{gathered} \tag{4.3.2.2}$$

An example of a gaussian x and gaussian xy 2d array is in figure, respectively, 4.3.1.4 and 4.3.1.5. and is the photonic counterpart of the electronic localization length which characterize the electron localization in random potentials. As has been observed firstly by Anderson[7], when the electrons are subjected to a defect's potential, their wavefunction is not free to propagate in the real space and is instead localized around the defect's position. In the same way, for any wave phenomenon that involves wave's scattering by a disordered medium, as may be for instance a photonic crystal subject to fabrication errors, the waves tends to localize around the defect. The wave's localization can then be used to enhance the electric intensity at the nanoscale. The localization length, as defined in equation 4.3.2.1 can be then used to measure the disordered induced enhancement effectiveness. Anyway, equation 4.3.2.1 is not clear about the condition under which this quantity has to be computed. To compute the localization length the system has firstly to be excited and then let go to a steady state, so the source must be switched of at a certain point. Indeed, the system can be effectively considered as made of coupled resonant cavities so, if the source was still on, it would force the cavities to oscillates to a frequency different from their natural one. An interesting feature of the participation ratio is that, no matter the kind of disorder present in the system and no matter what kind of source used, it always shows an initial series of peaks related to the transient induced by the source and then, once the source is off, it oscillates around an average value with an harmonic-like behaviour, as evident in figure 4.3.2.1. This is evident once figure 4.3.2.1 is compared

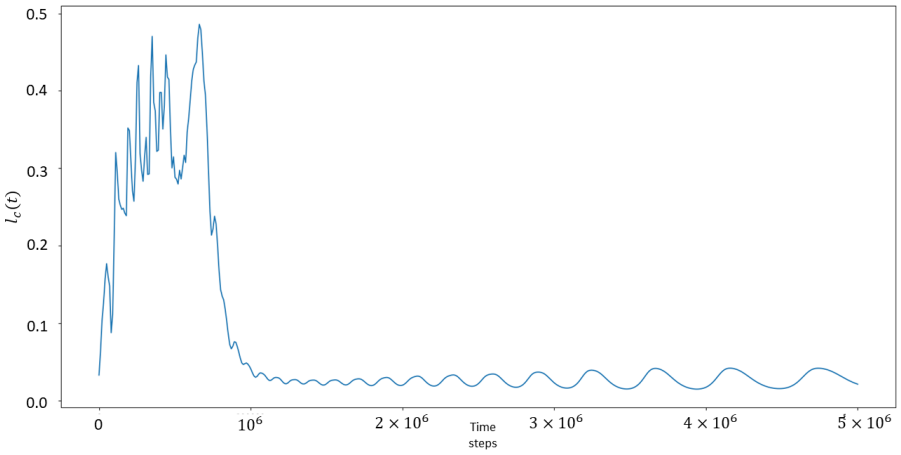

Figure 4.3.2.1:
Participation ratio $l_c(t)$ as a function of time of a single 2d binary array of nanopillars illuminated by a single pulse source whose central wavelength is at 500 nm. The participation ratio is computed every 1000 time steps.

with figure 4.3.2.2 where the participation ratio in time is shown for each disordered system. Being

so, what is of actual interest is its average, steady state value which must then be averaged over many realization of the same disorder. Therefore, fist the participation ratio is computed over many realization of the same disordered system numerically integrating the electromagnetic energy, computed by mean of the FDTD software

$$l_c(t) = \frac{(\int_V \mathcal{E}(t))^2}{V \int \mathcal{E}^2(t)} \approx \frac{(\sum_{[i,j]\in\, green\ box} \mathcal{E}[i,j,t])^2}{V \sum_{[i,j]\in\, green\ box} \mathcal{E}^2[i,j,t]}$$

Then, for each realization of any geometry the participation ratio has been averaged in time as

$$l_c = \frac{1}{N\Delta t} \sum_{i=1}^{N} l_c(t)$$

where N is the number of sample. Generally, a sample's frequency of 1/1000 time step is enough to achieve a good precision. The last step is to compute the microcanonical average over the realizations of a given disordered system to get the microcanonical participation ratio, which is a measure of how disorder and randomness affect the system. In the case of the binary array, the averaged participation ratio has been computed over 20 realizations per each values of p ranging from 0.05 to 0.95 in steps of 0.05. In the ternary case, 20 realization for each values of p_1 and p_2 such that $p_1 + p_2 \leq 1$ has been simulated. For the gaussian x and gaussian xy disorder 20 realization for each value of σ ranging from 5 nm to 25 nm have been used to compute the participation ratio. In the last two kind of system, the choice of the range of sigma is not random. Indeed, 5 nm is the minimum standard deviation due to nanofabrication's techniques that can be achieved while at 25 nm there is a concrete chance that the two pillars overlap, as shown in figure 4.3.1.4.

It is now time to discuss the actual localization length for each system. First, the binary array. The localization length reaches its minimum around p=0.68 and this minimum doesn't actually depends on the wavelength of the source. Indeed, in the top left of figure 4.3.2.3 it is possible to observe how the the minimum is absolutely constant as the wavelength changes. The behaviour is confirmed by the computation of the microcanonical participation ratio for the same system illuminated by a single pulse source, which is a broadband source in the wavelength domain. As can be seen from the top right of figure 4.3.2.3, the participation ratio reaches its minimum in 0.68 also in this case. Since a single pulse source can be decomposed as a superposition of properly weighted plane waves, p equal 0.68 must be a minimum at all frequencies being the minimum for the sum of the frequencies. This seems to point out that the capability of the system of confining the electromagnetic field at the nanoscale does not depends on the frequency of the exciting field but only on the degree of disorder of the system. Lately, it is worth to say that the binary localization length has a nice bell shape, quite similar to the 1d binary chain[10] Then the localization length has been computed for a 2d ternary array. The ternary array is perhaps the most promising because shows the smallest localization length. Since the geometrical and computational feature has been kept fixed for all the simulations, the localization length of the four systems can be compared. As can be seen from image4.3.2.4, the localization length reaches its minimum of about 0.018, against the roughly 0.021 reached by the binary array, which is a clue that this kind of disorder may perhaps be the most suited for the enhancement of the electric field at the nanoscale as well as for the enlargement of its spectrum's broadness. Unluckily, due to some resource's limitations, the computation of the localization length with plane wave source has not been possible. Nevertheless, some hypothesis, based on the behaviour of the other systems analyzed, can be made. For instance, the expectation is to have some small fluctuation in the argmin of the localization length at each frequency, but

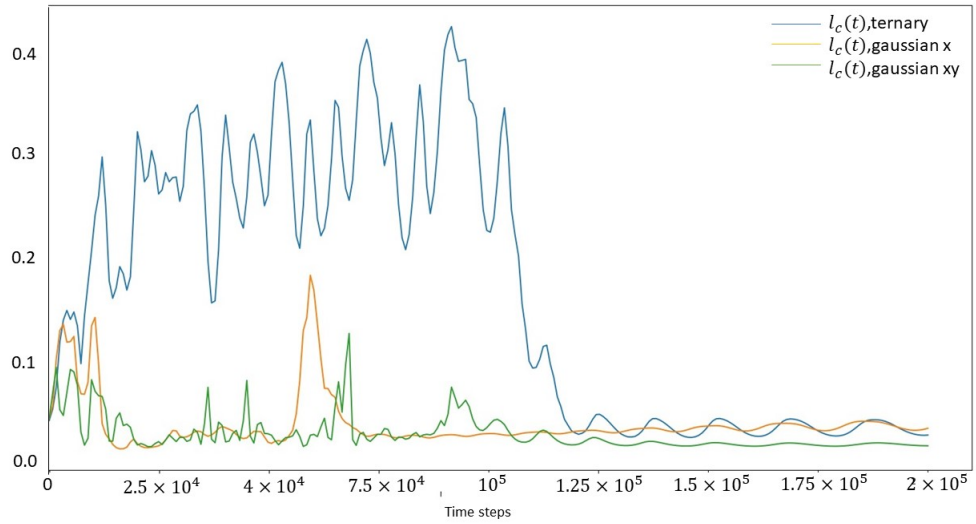

Figure 4.3.2.2:
Participation ratio computed for a 2d gaussian x, gaussian xy and ternary array. Comparing the participation ratio of the four types of disorder, it it possible to observe the generality of this behaviour once the system enter in the stationary state.

this should be related to the small number of samples used for the microcanonical average rather than to any strong system's dependence on the impinging plane wave's wavelength.
The next system to be analyzed is the 2d gaussian x array. In this case the parameter that control the amount of disorder is the standard deviation of the probability distribution determining the coordinate along the y axis of each nanopillar which ranges from 5 to 25 nm in step of 1 nm. As can be seen in the top right image of figure 4.3.2.5, the smaller localization length reached is about 0.021, larger than the localization length of the ternary case. It is worth to be noticed that the localization length reaches, for some wavelength, a value smaller than the minimum found in the ternary case, as shown in left bottom image of figure 4.3.2.5 but the localization length given by a broadband source is the one that actually matter. Nevertheless, the minimum gaussian x localization length is already smaller or equal than the binary case and as consequence, from the point of view of the enhancement of the electromagnetic field at the nanoscale, the results obtained by a 2d binary case may be equivalent to those of a 2d gaussian x array, which may be easier to fabricate. Anyway, it seems that the localization length decreases as σ increases, so it is likely to expect a value of σ such that the gaussian x array's localization length is smaller or equal than the ternary one. Once again, the localization length seems to be quite unaffected by the wavelength of the impinging source. As can be seen in the bottom right of figure 4.3.2.5, the $\sigma_{min} = argmin_\sigma\{\langle l_c(\sigma,\lambda)\rangle_m\}$ does not change considerably in frequency, and the small change of 1 nm is well explained considering the variance of this quantity and the fact that here the disorder has a continuous and not discrete nature. Perhaps, if the number of sample used to perform the microcanonical average was larger, this small variation of σ_{min} would have disappeared. In any case, a 1 nm variation is small enough

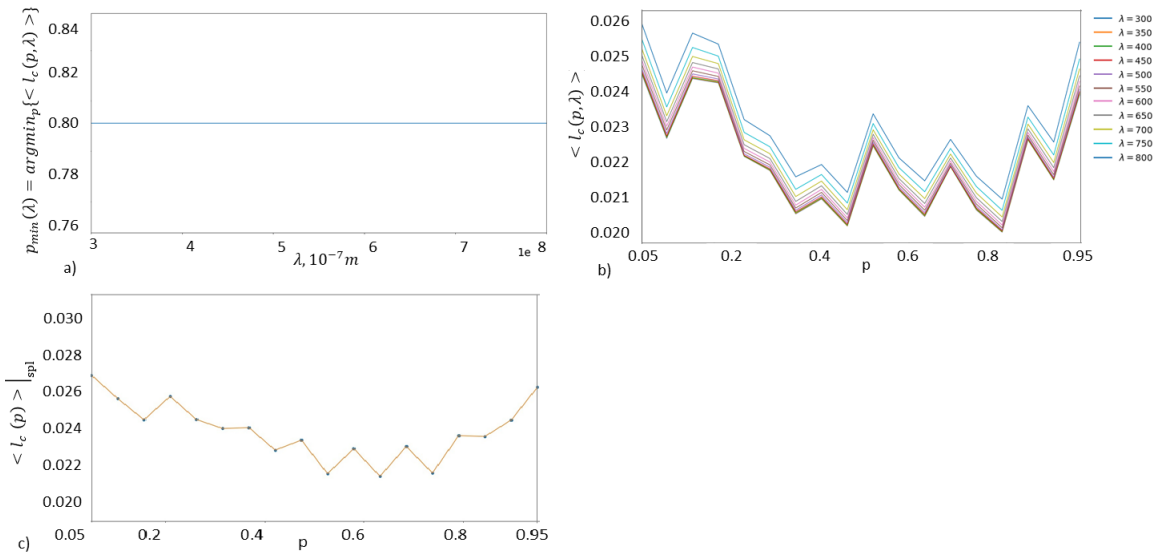

Figure 4.3.2.3:
2d binary array
a) $argmin_p\{\langle l_c(p,\lambda)\rangle_m\}$. Even if, for logistic reasons, the number of sample to perform the microcanonical average has been reduced from 20 to 10 for the computation of $\langle l_c(p)\rangle_m$ at single frequencies the minimum remains constant and coincides with the one found computing $\langle l_c(p)\rangle_m$ for the same system excited by a single pulse source;
b) $\langle l_c(p)\rangle_m$ computed exciting the system using a monochromatic plane wave a with a wavelength ranging from 300 to 800 nm with a step of 50 nm switched off after 5 optical cycles. It is clear that the behaviour of the localization length does not depends on the impinging wavelength but only on the degree of disorder of the system. Moreover it is clear how almost ordered systems, for p=0.05 and p=0.95, are much less effective in confining and condensing the electromagnetic field than highly disordered systems. It may be observed, indeed, how the lowest values for the localization length are obtained for values of p ranging from about 0.05 to about 0.07. Remarkably, this behaviour is so robust that even an averaging over a modest number of realization for each wavelength and p is enough to show it;
c) localization length computed using as source a single pulse with a central wavelength of 500 nm and a waist of 300 nm.

to be neglected, when it come to nanofabrication where the minimum standard deviation for the center of such nanopillar would be at least of 5 nm.
Finally, the last system to be discussed is the 2d gaussian xy array. As in the previous case, the parameter that control the disorder is σ ranging from 5 to 25 nm in steps of 1 nm, whose effect of the nanopillars center coordinate's is explained in equation 4.3.2.2. As can be seen from the top right image of figure 4.3.2.6, the localization length of the gaussian xy case computed under a broadband source doesn't change significantly but is even more fluctuating than the gaussian x case. This is not surprising, since the number of samples used to compute the microcanonical average

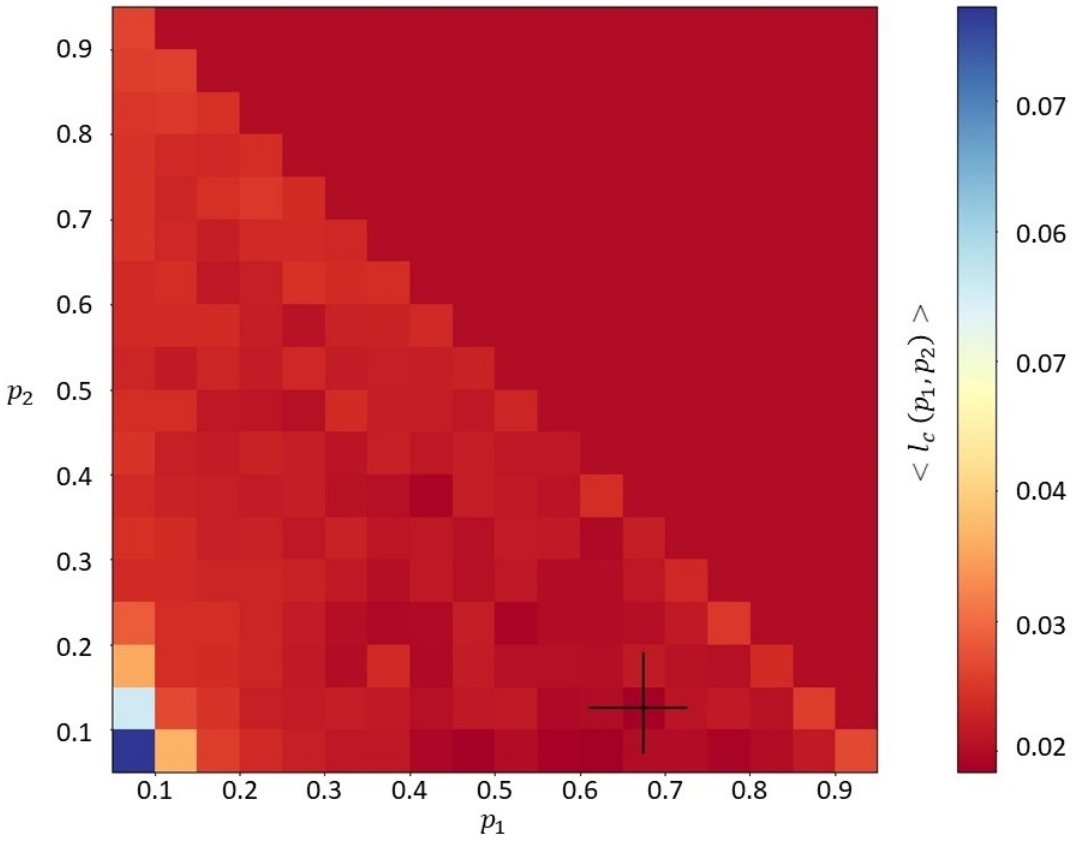

Figure 4.3.2.4:
Participation ratio computed for a 2d ternary array. The allowed couples p_1, p_2 are those such that $p_1 + p_2 \neq 1$. All the remaining pixels, namely the upper half of the square, are set to a meaningless standard value. It is clear how the increase of disorder decreases the localization length. Indeed, the pixels corresponding to the couple such that there is a small disorder, as can be when $p_1 + p_2 = 1$ or when there is absolute predominance of a single type of nanoparticle, are much lighter than those in which there is a good mix of nanoparticles.

is kept constant to 10 for logistical reasons but the disorder of the system is further increased. Just as in the gaussian x case, it is true that the gaussian xy localization length reaches, for some wavelength of the impinging wave, a much smaller localization length than the ternary case one but, as before, it is the result shown in the top right image of figure 4.3.2.6 that matters. Anyway, the general trend of $\sigma_{mim} = argmin_\sigma\{< l_c(\sigma, \lambda >_m\}$ which is mostly unaffected by the wavelength is shown in the bottom right image of figure 4.3.2.6. The fluctuations shown by σ_{min} may once again be explained by the small number of samples used to compute the microcanonical average. The only case in which the system does not follow the general trend is for an impinging plane wave of wavelength equal to 700nm. In this case, σ_{min} is found to be at about 14 nm but, as can been seen from figure 4.3.2.7, the difference between $< l_c(\sigma = 14) >= \sigma_{min}|_{\lambda=700nm}$ and $< l_c(\sigma = 24) >$

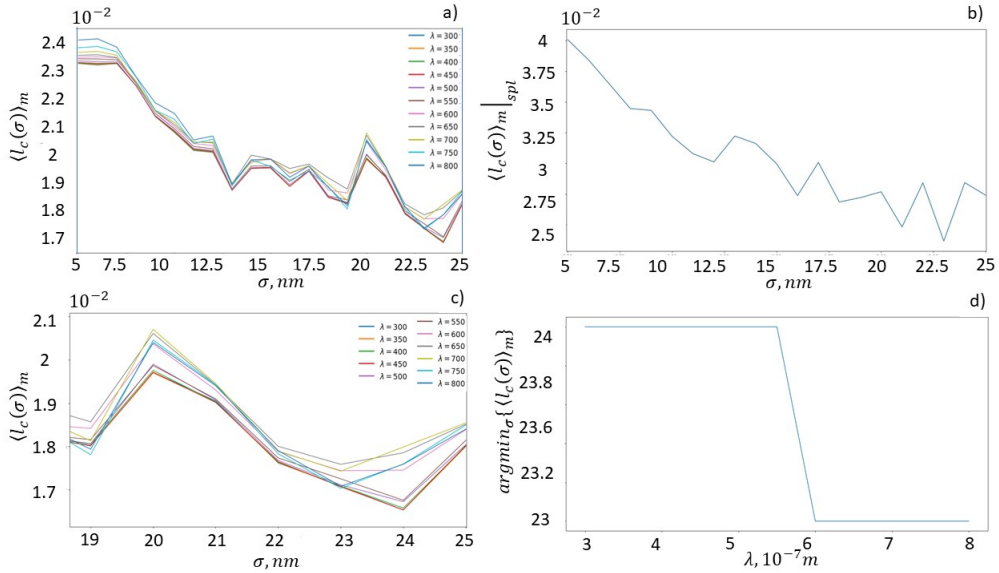

Figure 4.3.2.5:
2d gaussian x array.
a) localization length computed for a plane wave source whose wavelength ranges from 300 to 800 nm in step of 50 nm and switched off after 5 optical cycles. It is clear the general trend which depends only on the quantity of disorder introduced in the system and not on the incident wavelength;
b) localization length computed for single pulse source whose central wavelength is in 500 nm and whose waist is of 300 nm. In this case the minimum of the localization length is for $\sigma_{min} = 23nm$, which is in the range found computing the localization length at each wavelength. Perhaps, this value of σ_{min} should be the one to be used for a fabrication since takes into account of the superposition of all the wavelength;
c) detail of the localization length computed at each wavelength;
d) $argmin_\sigma\{\langle l_c(\sigma,\lambda)\rangle_m\}$. The small fluctuation observed in this case is related to the small number of sample used for the computation of the localization length.

is the 0.54 % of σ_{min} hence this small deviation is likely explained by the small number of samples used for the microcanonical average.
In any case, the overall minimum localization length of the gaussian xy array is pretty much the same as the gaussian x and binary array's localization length, hence suggesting that the instrumental errors due to the nanofabrication of such system, which is practically a metasurface[13] in the visible and near infrared spectrum, can be effectively used to tune the electromagnetic properties of the these 2D array. Perhaps, a good strategy may be firstly to find the optimal $sigma_{min}$ and then to fabricate the array with a σ_{ext} such that

$$\sigma_{min} = \sigma_{nano} + \sigma_{ext}$$

where σ_{nano} is the standard deviation due to the nanofabrication process.
In conclusion, the ternary array seems to be the one with the smallest overall localization length but it is also quite difficult to realize. Instead, a good substitute is the 2d gaussian x or gaussian

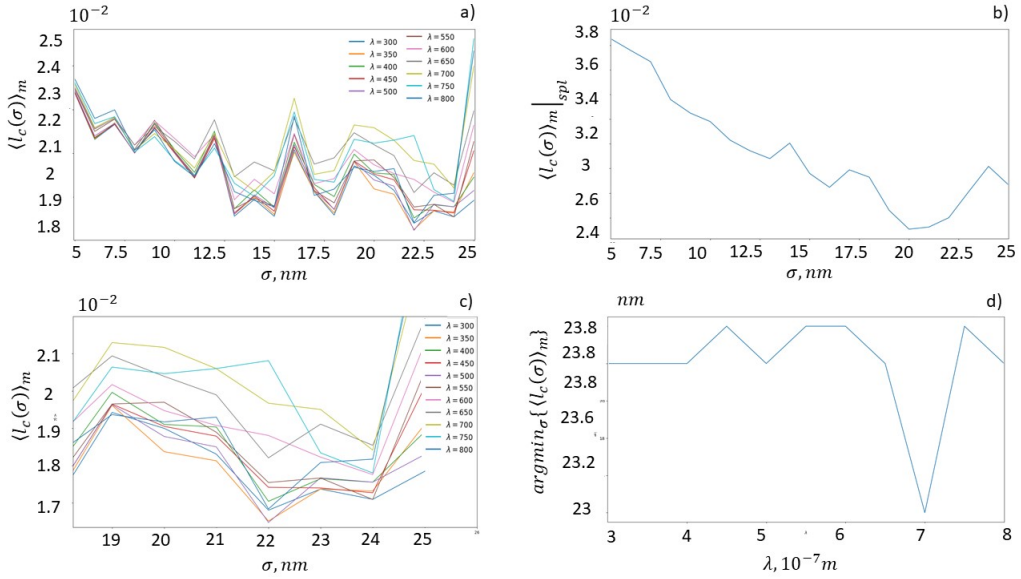

Figure 4.3.2.6:
2d gaussian xy array
a) localization length computed for impinging plane waves whose wavelength ranges from 300 to 800 nanometers in step of 50 nanometers switched off after 5 optical cycles. The general trend follows quite closely the behaviour of the localization length obtained using a single pulse source but it is much more subject to fluctuation. These fluctuations may, indeed, be related to the small number of samples using to compute the microcanonical average;
b) localization length computed for a single pulse source with σ ranging from 5 to 25 nanometers. Its minimum is reached for σ smaller than maximum allowed standard deviation, suggesting that when the overlap between two nanopillars is too likely, the effective number of optical cavities decreases as well as the effective average center to center distance. In this case the characteristic length of the array is too large with respect to the smallest of the wavelength which may propagate more freely in this case, reducing the amount of energy transferred to the system;
c) detail of the localization length computed with the a plane wave source;
d) $\sigma_{min}(\lambda) = argmin_\sigma\{\langle l_c(\sigma,\lambda)\rangle_m\}$. σ_{min} is quite constant unless the case of $\lambda = 700nm$. As explained in the main text, this is much likely due to the small number of sample used to perform the microcanonical average rather than due of any dependence of the σ_{min} on the impinging wavelength
.

xy array which shows an overall localization length smaller or equal than the one of the binary case but are of simple realization.

4.3.3 Hot electron generation rate for 2d disordered arrays

Once the parameters that minimize the localization length, hence theoretically enhancing the electromagnetic field, for each kind of disorder have been found, the last and natural step is to compute the hot electron generation rates for these conditions summarized in table 4.1 In order to save

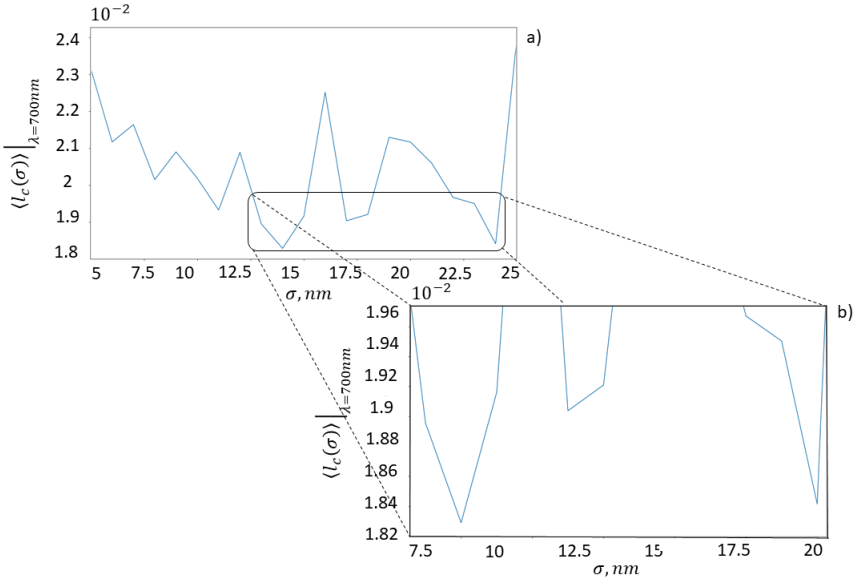

Figure 4.3.2.7:
a) localization length computed for a plane wave source of wavelength=700 nm switched off after 5 optical cycles;
b) detail of the above top left image. It is clear how small is the differences between $\langle l_c(\sigma = 14nm)\rangle_m$ and $\langle l_c(\sigma = 24nm)\rangle_m$

2d array	parameter's value
binary	p=0.68
ternary	$p_1 = 0.1,\ p_2 = 0.68$
gaussian x	$\sigma = 23nm$
gaussian xy	$\sigma = 20nm$

Table 4.1: localization length argmin for each 2d array's type

computational time and resources, the normal to the surface electric field and the hot electron generation rate has been computed using a method different than equation 4.1.0.1, for which it is needed a simulation for every wavelength ranging from 300 nm to 800 nm. In this case, a single pulse source whose central frequency is at 500 nm and whose waist is of 300 nm has been used to excite the system. The electromagnetic field has been recorded in time on 10 equispaced points on each particle belonging to the array, as shown in figure 4.3.3.1. Once the simulation is done, each of the recorded field has been projected on the normal to the surface versor in that point and Fourier transformed. Then the intensity of the normal electric field has been computed as

$$I(\mathbf{r}, \omega) = \mathcal{F}[E_n(\mathbf{r}, t)](\omega)\mathcal{F}^*[E_n(\mathbf{r}, t)](\omega)$$

The last step is the integration over the particles surface, which numerically is obtained just by summing up all the transformed field. In this way, for each disorder realization has been needed only one simulation, reducing the amount of simulation needed to 80, 20 for each different kind

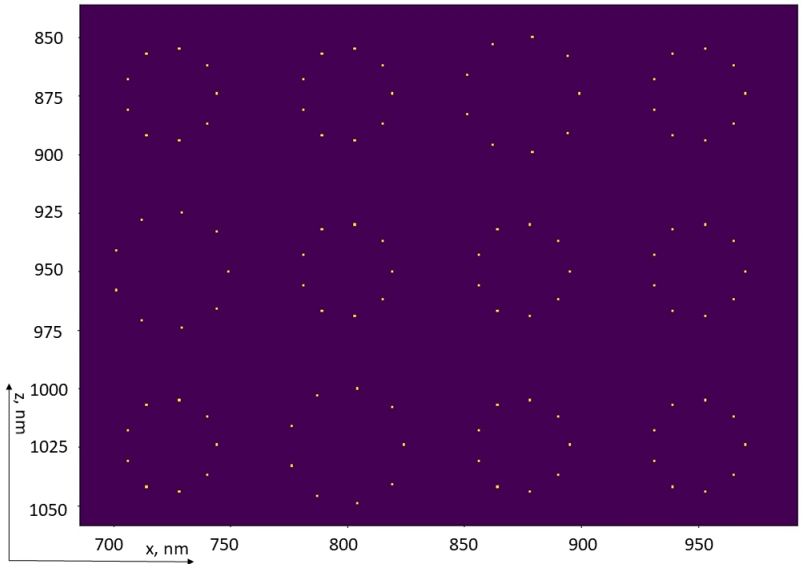

Figure 4.3.3.1:
probe disposition in space to record the electromagnetic field on the surface of the nnanopillars

of disorder, against the 2000 that would have been needed using the former procedure. From the point of view of the intensity spectrum, the results are quite remarkable, as can be seen in figure. Indeed, the four systems show a broad intensity spectrum, in particular in the red and near infrared range. This broadness is completely due to the introduction of disorder in the system and is quite similar in the four cases, as shown in figure 4.3.3.2. It confirms that the properties of a binary or ternary array may be approximately replicated using a gaussian x or gaussian xy array and viceversa. Indeed, this feature is not trivial since it allows a good flexibility when it comes to the fabrication of such a structure, even if, in general the ternary array is the one that shows the better performances.
The hot electron generation rates are also quite similar to each other and all show a greater rate in the red a near infrared part of the visible spectrum rather than in blue and violet part. This behaviour is completely due to quantum effects and can be modified by the choice of material and by the choice of the single particle geometry, but it is not affected by the type of disorder. It is indeed known that cavities made of nanoparticles present a red shift of the resonance peak compared to the single particle case which is a function of its geometrical features[9]. If the averaged intensity spectrum of 2d binary arrays is interpreted as a weighted superposition of peaks due to single cavities, then it is reasonable that the 2d array's intensity spectrum become broader in the red and infrared frequency range as all the peaks are shifted in that direction. Therefore the only way to increase the broadness of the hot electron generation rate in the visible spectrum is to choose a material and a single particle geometry such that the single particle resonance peak's wavelength is in the low wavelength range. For instance, Govorov and collaborators[14] have reported that silver is much more effective than gold for the hot electron generation rate and the cubic geometry has shown the best performances among all the studied single particle geometry. However, it is

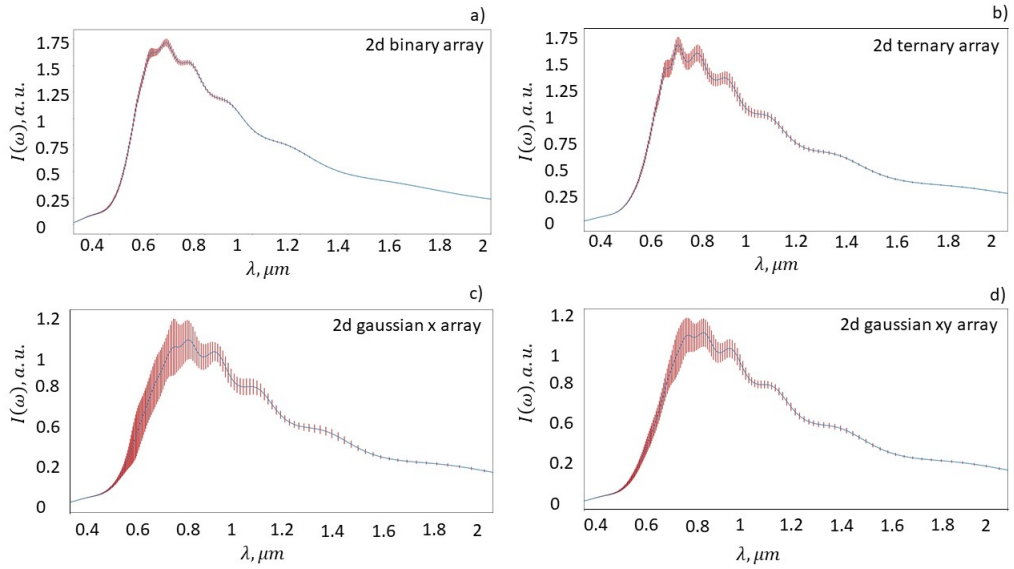

Figure 4.3.3.2:
a) field intensity's microcanonical average of the 2d binary array;
b) field intensity's microcanonical average of the 2d ternary array;
c) field intensity's microcanonical average of the 2d gaussian x array;
d) field's intensity of the microcanonical average of the gaussian xy array.
The red lines represent the standard deviation computed over the different realization of the same disordered system at each wavelength. Once again, the effect of the small number of samples used for the microcanonical average can be observed: the binary case is the only case that does not present a large standard deviation due to the small its intrinsically small fluctuation compared to the other cases. It is moreover clear how the standard deviation increases as the disorder increases, as it is much larger for the gaussians array whose disorder is continuous than for the binary of ternary array whose disorder is discrete. The four surface DOS spectrum can be compared since all of them are normalized to the same value

clear that the role of disorder is to break down the cavities coupling allowing the spectrum to be a weighted superposition of many different contributions but it has no way to blue-shift the cavities peak's frequency.

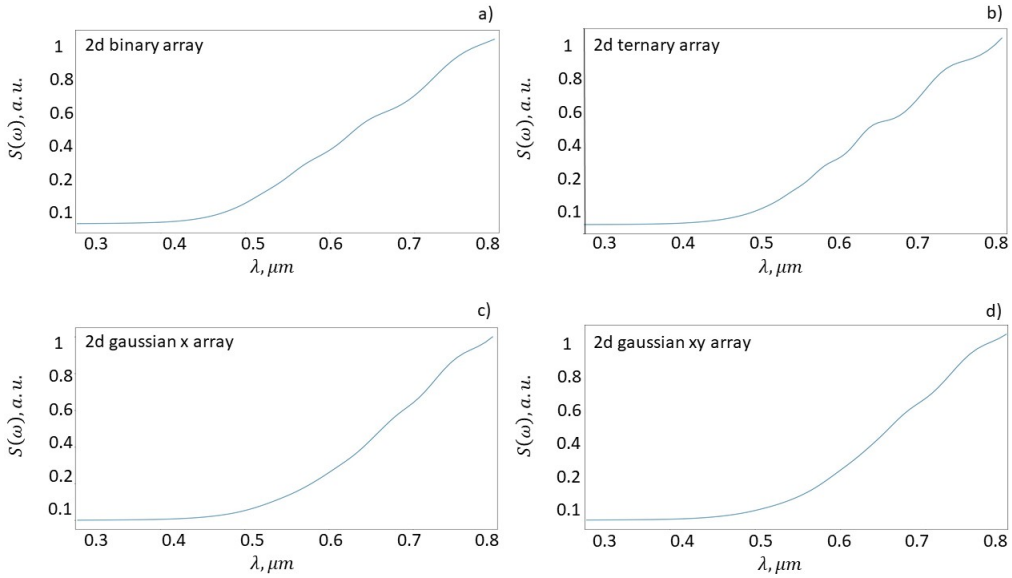

Figure 4.3.3.3:
a) averaged hot electron generation rate for the 2d binary array;
b) averaged hot electron generation rate for the 2d ternary;
c) averaged hot electron generation rate for the 2d gaussian x array;
d) averaged hot electron generation rate for the 2d gaussian xy array;
The four generation rates are quite similar to each other and show a broad generation rate in the close infrared and red part of the solar spectrum. The y-axis is in arbitrary units in all the plots.

Chapter 5

Conclusion

The theoretical background for the study of the nanoparticle's hot carriers generation rate has been recalled as well as the numerical tools needed to simulate a generic electromagnetic system. In this framework four geometries, the sphere, the ellipsoid, the cube and the cylinder, has been analyzed by mean of FDTD simulation and their power density spectrum computed. Among the others, the cubic geometries has appeared as the one presenting the most broad intensity and hot electron generation rate but the cylindrical one has been chosen since it is the simplest to nanofabricate with a good control of its the geometrical features.
The next natural step has been the study of 2d arrays of nanoparticles, which are of real interest when it comes to a massive hydrogen generation. Among all possibilities, 2d arrays characterized by different kind of disorder has been studied in order to understand weather the randomness can be exploited to increase the hot electrons generation rate. The effect of disorder has been characterized by the localization length whose study has allowed to find the amount of disorder that maximize the performances of the different disordered arrays. It is worth noticing that the localization length has show a robust behaviour with respect to the wavelength of the impinging wave, hence showing to be affected only by the particular kind of disorder present in the system. The analysis of the computed surface photonic DOS and hot electron generation rate for such nanostructures has shown that both these two quantities both greatly benefit from a controlled introduction of disorder in the system.
In conclusion, the control of disorder is a new promising way to achieve performances that ordered structure could never achieve through a controlled break of collective behaviour and geometrical constants of the system.

Bibliography

[1] Crisanti Andrea. *Products of random matrices in statistical physics*. 1993.

[2] A Tafffdfffdfffdove. "Contents". In: *Computational Electrodynamics: The Finite-Differences Time-Domain*. 2nd ed. Boston: Artech House, 1998. ISBN: 1-58053-076-1.

[3] Mark L. Brongersma, John W. Hartman, and Harry H. Atwater. "Plasmonics: Electromagnetic Energy Transfer and Switching in Nanoparticle Chain-Arrays Below the Diffraction Limit". In: *MRS Proceedings* 582.24 (1999), H10.5. ISSN: 1946-4274. DOI: 10.1557/PROC-582-H10.5. URL: http://journals.cambridge.org/abstract%7B%5C_%7DS1946427400639556.

[4] International Energy Agency. "Hydrogen Production and Storage. R&D Priorities and Gaps". In: *Hydrogen Implementing Agreement* 13 (2006), pp. 392–392. ISSN: 03603199. DOI: 10.1016/0360-3199(88)90106-1. URL: http://linkinghub.elsevier.com/retrieve/pii/0360319988901061.

[5] Stefan Alexander(Centre for Photonics Mayer, Photonic Materials, and UK) Department of Physics, University of Bath. *Plasmonics: Fundamental and Applications*. Springer, 2007. ISBN: 978-0387-33150-8.

[6] U Rössler. *Solid state theory: An introduction*. 2009. ISBN: 9783540927617. URL: http://books.google.com/books?hl=en%7B%5C&%7Dlr=%7B%5C&%7Did=qRsH7TWDjYEC%7B%5C&%7Doi=fnd%7B%5C&%7Dpg=PR17%7B%5C&%7Ddq=Solid+State+Theory+an+Introduction%7B%5C&%7Dots=ZSnnEyp4OI%7B%5C&%7Dsig=AYSwe0kHml2gt0Oq-e1Mc-A-ErI.

[7] Mordechai Segev, Yaron Silberberg, and Demetrios N. Christodoulides. "Anderson localization of light". In: *Nature Photonics* 7.3 (2013), pp. 197–204. ISSN: 17494885. DOI: 10.1038/nphoton.2013.30.

[8] Hui Zhang and Alexander O. Govorov. "Optical generation of hot plasmonic carriers in metal nanocrystals: The effects of shape and field enhancement". In: *Journal of Physical Chemistry C* 118.14 (2014), pp. 7606–7614. ISSN: 19327455. DOI: 10.1021/jp500009k.

[9] Kristian L. Göeken, Vinod Subramaniam, and Ron Gill. "Enhancing spectral shifts of plasmon-coupled noble metal nanoparticles for sensing applications". In: *Physical Chemistry Chemical Physics* 17.1 (2015), pp. 422–427. ISSN: 14639076. DOI: 10.1039/c4cp03739a.

[10] Juan Sebastian, Totero Gongora, and Andrea Fratalocchi. *Encyclopedia of Nanotechnology*. 2016. ISBN: 978-94-017-9779-5. DOI: 10.1007/978-94-017-9780-1. arXiv: arXiv:1011.1669v3. URL: http://link.springer.com/10.1007/978-94-017-9780-1.

[11] Lucas V. Besteiro et al. "Understanding Hot-Electron Generation and Plasmon Relaxation in Metal Nanocrystals: Quantum and Classical Mechanisms". In: *ACS Photonics* 4.11 (July 2017), pp. 2759–2781. ISSN: 2330-4022. DOI: 10.1021/acsphotonics.7b00751. arXiv: 1707.06125. URL: http://pubs.acs.org/doi/10.1021/acsphotonics.7b00751%20http://arxiv.org/abs/1707.06125.

[12] Xiang Tian Kong, Zhiming Wang, and Alexander O. Govorov. "Plasmonic Nanostars with Hot Spots for Efficient Generation of Hot Electrons under Solar Illumination". In: *Advanced Optical Materials* 5.15 (2017). ISSN: 21951071. DOI: 10.1002/adom.201600594.

[13] *Electromagnetic_metasurface @ en.wikipedia.org*. URL: https://en.wikipedia.org/wiki/Electromagnetic%7B%5C_%7Dmetasurface.

[14] Alexander O Govorov, Hui Zhang, and Yurii K Gun 'ko. *Theory of Photoinjection of Hot Plasmonic Carriers from Metal Nanostructures into Semiconductors and Surface Molecules*. DOI: 10.1021/jp405430m. URL: https://pubs.acs.org/doi/pdf/10.1021/jp405430m.